



ORIGINAL PAPER

Ali Akbar Jahanitabar · Vahid Lotfi

Formulation and efficient implementation of coupled anisotropic damage-plasticity model for plain concrete

Received: 8 December 2023 / Revised: 30 March 2024 / Accepted: 9 April 2024 / Published online: 23 May 2024
© The Author(s), under exclusive licence to Springer-Verlag GmbH Austria, part of Springer Nature 2024

Abstract The formulation and finite element implementation of an efficient anisotropic damage-plasticity model is proposed to simulate the nonlinear behavior of plain concrete at small strains. The model's formulation is presented first; then, the implementation strategy is described. A stress-based yield criterion and two damage criteria are used to determine the nominal stress tensor. Using two damage tensors automatically accounts for the stiffness recovery in transition from tension to compression and vice versa. Some numerical issues are addressed, and the remedy is proposed. The deficiencies of existing anisotropic damage-plasticity models for plain concrete are also identified and discussed. Different alternatives for the general formulation of damage procedure are presented and compared. Three methods are introduced for calculation of damage hardening parameters and compared in terms of efficiency. The extension of the model to viscoplastic behavior is carried out using the frequently-used Duvaut–Lions viscoplasticity theory. Moreover, the formulation is extended to include the large crack in monotonic and cyclic loading, which improves the response of material under large values of strain. The model is included in an in-house finite element software previously developed by the authors. It is validated, and its efficiency is evaluated by comparing the software results with a set of experimental tests, such as monotonic uniaxial and biaxial tests, cyclic uniaxial tests, and some structural single-mode and mixed-mode tests.

List of symbols

\bar{c}^{\pm}	Isotropic hardening functions
\mathbf{E}	Damaged elastic rigidity tensor
$\bar{\mathbf{E}}$	Undamaged elastic rigidity tensor
f	Plastic yield surface
f_0^+, f_0^-, f_{b0}	Initial yield strengths in uniaxial tension and compression and biaxial compression
F^P	Plastic potential function
g^{\pm}	Damage yield surfaces
\bar{G}	Effective shear moduli
G_f^{\pm}	Fracture energy
H	Heaviside step function
\bar{I}_1	First invariant of the effective stress tensor
\bar{J}_2	Second invariant of deviatoric effective stress tensor
\bar{K}	Effective bulk moduli
K^{\pm}	Damage hardening functions

K_0^\pm	Damage initiation threshold
l^*	Characteristic length scale
\mathbf{M}^{-1}	Inverse of the damage effect tensor
$n^{(j)}, \hat{\sigma}^{(j)}$	j th eigenvector and eigenvalue of the stress tensor
\mathbf{P}^\pm	Stress projection tensors
Q, b, h, B^\pm, q^\pm	Material constants
r	Weight function
\mathbf{s}	Deviatoric stress tensor
\mathbf{Y}^\pm	Damage driving forces
α_μ	Interpolation factor
Δt	Characteristic time increment
δ	Kronecker delta
$\boldsymbol{\varepsilon}$	Nominal strain tensor
$\boldsymbol{\varepsilon}^e, \boldsymbol{\varepsilon}^p$	Elastic and plastic strain
$\bar{\boldsymbol{\varepsilon}}_{\text{eq}}^{\pm p}$	Equivalent plastic strain
$\tilde{\boldsymbol{\varepsilon}}^p$	Intermediate plastic strain
$\boldsymbol{\varepsilon}^{vp}$	Viscoplastic strain tensor
κ^\pm	Plastic hardening parameters
$\dot{\lambda}^p, \dot{\lambda}^{d^\pm}$	Plastic and damage multipliers
μ	Viscosity parameter
$\boldsymbol{\sigma}$	Nominal stress tensor
$\bar{\boldsymbol{\sigma}}$	Effective stress tensor
$\hat{\bar{\boldsymbol{\sigma}}}$	Principal effective stress
$\bar{\boldsymbol{\sigma}}^{\text{tr}}$	Trial effective stress
$\tilde{\boldsymbol{\sigma}}$	Intermediate effective stress
$\boldsymbol{\varphi}^\pm$	Anisotropic damage tensors
φ_{eq}^\pm	Equivalent damage parameter
$\varphi^{\text{eq}, v}$	Viscous equivalent damage variable
φ_{cr}	Large crack threshold
\square	Rate quantity

Abbreviations

IDPM	Isotropic damage-plasticity model
ADPM	Anisotropic damage-plasticity model
CMSD	Crack mouth sliding displacement

1 Introduction

Experiments show that when concrete is subjected to tensile and compressive loading, the increasing strain consists of an inelastic portion that does not recover in unloading. The recoverable part of strain can be formulated using the theory of elasticity, while the irrecoverable part can be described by plasticity theory. On the other hand, concrete is filled with microcavities and microcracks in the microscale. The degradation in strength and stiffness of material caused by these microdefects is called concrete damage, and its evolution is a result of nucleation, growth, and coalescence of microflaws. Furthermore, by increasing the strain, these irreversible microcracks join together and form localized macrocracks in the material. The well-known continuum damage mechanics has recently been introduced to simulate concrete damage and stiffness degradation.

The nonlinear behavior and strain softening of concrete are mainly the results of these irreversible strain and stiffness degradation effects. Numerical reproduction of this nonlinear behavior of concrete has received considerable attention in the literature. However, predicting the post-peak behavior of quasi-brittle materials is a challenging task. A successful numerical model should be able to represent the most important characteristics of concrete material, namely irreversible deformations, inelastic volumetric expansion and material crushing in compression, growth of microcavities and microcracks in tension, large crack formation, stiffness degradation, and stiffness recovery in cyclic loadings. Although the present study focused only on plain concrete, it is

noteworthy that some of the mechanical characteristics that govern the behavior of plain concrete become much less significant in reinforced concrete. Plain concrete is inherently brittle and has a low tensile strength compared to its compressive strength, making it very weak in tension. Reinforced concrete, on the other hand, exhibits different behavior due to the presence of steel bars that carry the tensile loads and increase the ductility of material. The tensile strength of steel bars improves the composite material's ability to resist cracking under tensile and bending loads. Consequently, the fiber reinforcements are commonly used in the construction industry to improve the ductility and tensile performance of concrete. However, analyzing the behavior of reinforced concrete is a more complex problem than analyzing plain concrete behavior and is beyond the scope of this study.

The theory of plasticity has been extensively adopted by researchers, up to now, in modeling the nonlinear behavior of plain concrete [1–5]. Plasticity models are generally capable of addressing irreversible deformation in concrete. However, the important property of stiffness degradation cannot be included in classical continuum plasticity. In contrast, the continuum damage models are able to successfully reproduce the stiffness degradation of concrete. However, they cannot simulate irreversible deformations observed in experiments. They are also limited to tensile and low confined compression stress in most cases. Continuum damage mechanics has been widely used in recent years to predict material failure [6–28].

Considering the shortcomings of plasticity and damage models, researchers combined these two models to develop powerful plastic damage models, which can overcome the mentioned drawbacks and describe essential features of concrete material. These models are mainly based on isotropic hardening plasticity and either isotropic or anisotropic damage models. The isotropic damage-plasticity models (IDPM) usually employ one or two variables to describe the influence of damage initiation and growth. These scalar variables represent the average microdefects and indicate overall degradation in the material. In recent years, the IDPM models have been extensively adopted in the literature [29–50].

The IDPM models assume damage evolution to be isotropic, which is not physically meaningful for concrete material that exhibits anisotropic behavior. This is because the microdefects in concrete are highly oriented. Cracks, in particular, have an orientation-dependent nature and grow perpendicular to the maximum tensile stress direction. In terms of formulation, the damage evolution is a function of stress, which is a tensor quantity and orientation dependent. Therefore, the development of an anisotropic damage model for concrete is essential. The coupled plasticity-microplane damage models and the anisotropic damage-plasticity models (ADPMs) have been developed in recent years to reflect the orientation-dependent nature of damage in the analysis.

The ADPM models use the damage tensors instead of scalar variables to describe material degradation. Hence, the effect of anisotropy can be well addressed in these models and more accurate results can be achieved, but the constitutive relations would be much more complex.

Park et al. [51] and Voyiadjis et al. [52] present the theoretical and numerical review of continuum damage mechanics and plasticity in the context of finite elements. They also included an extensive review of multiscale modeling in concrete, in which multiple models on different length scales are combined [53]. Cicekli et al. [54] proposed an ADPM model with two damage tensors for positive and negative parts of damage to predict the anisotropic behavior of plain concrete. They used a decoupled algorithm for calculation of effective stress and damage evolution. However, their local constitutive relations result in ill-posed initial boundary value problem for material softening and cannot guarantee the uniqueness of the solution. Moreover, the verification of the study is limited to a single element under uniaxial and biaxial monotonic loading. Voyiadjis et al. [55] and Voyiadjis et al. [56] also presented elasto-plastic-anisotropic damage formulations for concrete. They used the elastic strain energy equivalence hypothesis to transform from the effective to the nominal configuration. Abu Al-Rub and Voyiadjis [57] presented a nonlocal gradient-enhanced ADPM for plain concrete. They introduced two internal length scales as localization limiters of damage in tension and compression. Voyiadjis et al. [58] proposed an ADPM for quasi-brittle materials using the hypotheses of elastic and plastic strain energy equivalence.

Despite the remarkable studies on the ADPM, its limitations and shortcomings prevent its application on complex structures. Daneshyar and Ghaemian [59] compared three methods of IDPM, ADPM, and coupled microplane damage and plasticity model for simulating damage-induced anisotropy in plain concrete. They concluded that ADPM is unable to predict acceptable results in multiaxial loadings, and IDPM suffers from lack of accuracy. They addressed some drawbacks of ADPM and demonstrated that damage growth in different orientations is not an independent procedure with this model. Moreover, an unrealistic distribution of damage emerges and the maximum damage orientations remain unchanged during the analysis. They also performed some numerical tests with multidimensional loadings, which resulted in the ADPM's curve deviating from

the experimental one. Hence, they proposed the microplane-based damage formulation to overcome the shortcomings of existing models. However, using the microplane approach presents additional challenges in terms of computational cost [60] because of the large number of microplanes to be integrated on the surface of each integration point sphere in every element.

The aim of this study is threefold: first, to investigate and highlight the deficiencies of previous ADPMs for plain concrete and propose the appropriate remedy; second, to develop an efficient ADPM to overcome the mentioned limitations and shortcomings; and third, to present the finite element implementation strategy in detail. The proposed ADPM is derived under the assumption of small strains. A decoupled algorithm is used in the proposed model to combine the plasticity and damage procedures. An effective stress-based yield criterion and non-associative flow rule are used in the plasticity part. A fourth-order damage effect tensor is used to transform the effective (undamaged) stress to the nominal (damaged) stress. The effective stress tensor is decomposed into positive and negative parts to represent the unilateral effect. Consequently, two independent damage criteria and two damage tensors are defined. The spectral decomposition automatically considers the stiffness recovery in the transition from positive to negative stress and vice versa. The formulation is generalized to include large crack opening and closing. Hence, the formulation of large crack, presented by Lee and Fenves [61] for IDPM, is extended here to ADPM and embedded in the model. Moreover, the rate dependency is embedded in the model using the viscous model of Duvaut–Lions. In addition, the implementation methods are described in detail. Some numerical issues are discussed, and deficiencies of existing ADPMs are also revealed. Three methods are presented for the computation of damage hardening parameters and compared with respect to efficiency. Inspired by previous studies, three alternatives are also introduced and compared for the general formulation of the anisotropic damage model. An in-house finite element program is developed based on the proposed model. Using this simulation program, the paper investigates the efficiency and experimental verification of the model through different benchmark problems such as monotonic and cyclic uniaxial tests, monotonic biaxial test, and mixed-mode multidimensional structural tests.

The remainder of this paper is organized as follows: The study will begin by presenting the formulation of damage, decomposition of stress tensor, and plastic and damage yield criteria in Sect. 2. Different options for the general formulation of anisotropic damage are also discussed and compared in this part. Section 3 presents the implementation methods, including the modifications corresponding to large cracking and viscosity. Then, methods for calculation of plastic and damage hardening parameters are described, and the relations for plastic and damage multipliers are presented. Section 4 presents the validation results for a number of benchmark problems and Sect. 5 presents the conclusions.

2 Formulation

In this section, the main components of anisotropic damage and plasticity formulations are presented. A decoupled algorithm, including two steps of plasticity and damage, is used to update the nominal stress tensor. Both steps are formulated in the effective stress space. At the beginning of the plasticity step, the effective stress tensor is decomposed into positive and negative parts to consider the unilateral effect of concrete. Moreover, the transition from effective to nominal configuration is performed at the end of the damage step. The model is developed for three-dimensional space, and its theoretical basis is presented in the following.

2.1 A review on anisotropic damage

The relation between the nominal and the effective stress tensors can be expressed as:

$$\sigma_{ij} = M_{ijkl}^{-1} \bar{\sigma}_{kl} \quad (1)$$

where M_{ijkl}^{-1} is the inverse of the fourth-order damage effect tensor, which represents the effect of material damage and transforms the effective stress to the nominal stress, according to the history of damage. The strain equivalence or strain energy equivalence hypothesis can be used to derive the transformation relations. However, the strain equivalence hypothesis is adopted herein for simplicity in finite element implementation. This theory assumes that strains in the damaged and undamaged states are identical:

$$\varepsilon_{ij} = \varepsilon_{ij}^e + \varepsilon_{ij}^p = \bar{\varepsilon}_{ij}^e + \bar{\varepsilon}_{ij}^p = \bar{\varepsilon}_{ij} \quad (2)$$

Table 1 Available relations for $\mathbf{M}^{-1}/\mathbf{M}$ and the proposed relation of this study

1	[54, 57, 67]	$M_{ijkl}^{-1} = \frac{1}{2}[(\delta_{ij} - \varphi_{ij})\delta_{kl} + \delta_{ij}(\delta_{kl} - \varphi_{kl})]$
2	[55, 56]	$M_{ijkl} = \frac{1}{2}[(\delta_{kj} - \varphi_{kj})^{-1}\delta_{il} + \delta_{kj}(\delta_{il} - \varphi_{il})^{-1}]$
3	[68–70]	$M_{ijkl}^{-1} = \frac{1}{2}[(\delta_{ik} - \varphi_{ik})\delta_{jl} + \delta_{ik}(\delta_{jl} - \varphi_{jl})]$
4	[59]	$M_{ikjl} = \frac{1}{2}[(\delta_{ik} - \varphi_{ik})^{-1}\delta_{jl} + (\delta_{jk} - \varphi_{jk})^{-1}\delta_{il}]$
5	[66]	$M_{ijkl}^{-1} = \frac{1}{2}[(\delta_{im} - \varphi_{im})(\delta_{jm} - \varphi_{jm})\delta_{kl} + \delta_{ij}(\delta_{km} - \varphi_{km})(\delta_{lm} - \varphi_{lm})]$
6	Utilized relation	$M_{ijkl}^{-1} = \frac{1}{4}[(\delta_{ik} - \varphi_{ik})\delta_{jl} + (\delta_{jl} - \varphi_{jl})\delta_{ik} + (\delta_{il} - \varphi_{il})\delta_{jk} + (\delta_{jk} - \varphi_{jk})\delta_{il}]$

φ_{ij} in Table 1 is the anisotropic damage tensor.

The generalized Hooke's law is used to relate the effective stress tensor to the elastic strain tensor in the undamaged configuration:

$$\bar{\sigma}_{ij} = \bar{E}_{ijkl}\varepsilon_{kl}^e = \bar{E}_{ijkl}(\varepsilon_{kl} - \varepsilon_{kl}^p) \quad (3)$$

where \bar{E}_{ijkl} is the elastic rigidity tensor of the undamaged material which, for isotropic linear elastic materials, can be defined as follows:

$$\bar{E}_{ijkl} = 2\bar{G}I_{ijkl}^{\text{dev}} + \bar{K}\delta_{ij}\delta_{kl}, \quad I_{ijkl}^{\text{dev}} = \delta_{ik}\delta_{jl} - \frac{1}{3}\delta_{ij}\delta_{kl} \quad (4)$$

where \bar{G} and \bar{K} are the effective shear and bulk moduli, respectively. Furthermore, the nominal stress tensor can be defined as:

$$\sigma_{ij} = E_{ijkl}\varepsilon_{kl}^e \quad (5)$$

where E_{ijkl} is the fourth-order rigidity tensor of the damaged material and can be defined by employing Eqs. (1), (3) and (5):

$$E_{ijkl} = M_{ijpq}^{-1}\bar{E}_{pqkl}. \quad (6)$$

2.2 Fourth-order damage effect tensor M

One of the most important concerns in continuum damage formulation is employing a proper \mathbf{M}^{-1} (or \mathbf{M}), which accurately relates all components of the effective stress tensor to the nominal stress through Eq. (1). Depending on the form of \mathbf{M}^{-1} , the nominal stress tensor may be not symmetric after transformation in Eq. (1). Therefore, it is essential to employ an appropriate \mathbf{M}^{-1} that guarantees the symmetry of stress tensor after this transformation [51, 55, 62, 63]. Several relations are proposed for \mathbf{M}^{-1} (or \mathbf{M} in some references) in previous studies [54, 55, 59, 62–66]. Table 1 summarizes the available relations as well as the utilized relation in this paper. The shortcomings and drawbacks of different relations are demonstrated and discussed in the following.

2.2.1 First and fifth relation

$$\begin{aligned} \text{if } \varphi_{ij} = 0 \quad \text{then } M_{ijkl}^{-1} &= \delta_{ij}\delta_{kl} \\ \Rightarrow \sigma_{ij} = \delta_{ij}\delta_{kl}\bar{\sigma}_{kl} = \delta_{ij}\bar{\sigma}_{kk} &= \begin{pmatrix} 1 & 0 & 0 \\ 0 & 1 & 0 \\ 0 & 0 & 1 \end{pmatrix} (\bar{\sigma}_{11} + \bar{\sigma}_{22} + \bar{\sigma}_{33}) \end{aligned}$$

Hence, in a uniaxial compression test in the z direction, when the damage process is not started, the damage effect tensor turns the uniaxial experiment to a triaxial test. In this case, the effective and nominal stress tensors can be determined from the above as follows:

$$\bar{\sigma}_{ij} = \begin{pmatrix} 0 & 0 & 0 \\ 0 & 0 & 0 \\ 0 & 0 & \bar{\sigma}_{33} \end{pmatrix}, \quad \sigma_{ij} = \begin{pmatrix} \bar{\sigma}_{33} & 0 & 0 \\ 0 & \bar{\sigma}_{33} & 0 \\ 0 & 0 & \bar{\sigma}_{33} \end{pmatrix} \otimes$$

2.2.2 Second relation

$$\begin{aligned}
 M_{ijkl}^{-1}(\varphi = 0) &= I_{ijkl} \\
 M_{1313} &= \frac{1}{2}[(\delta_{13} - \varphi_{13})^{-1}\delta_{13} + \delta_{13}(\delta_{13} - \varphi_{13})^{-1}] = 0 \\
 M_{1331} &= \frac{1}{2}[(\delta_{33} - \varphi_{33})^{-1}\delta_{11} + \delta_{33}(\delta_{11} - \varphi_{11})^{-1}] = 0.5[(1 - \varphi_{33})^{-1} + (1 - \varphi_{11})^{-1}] \\
 &\Rightarrow M_{1313} \neq M_{1331}.
 \end{aligned}$$

2.2.3 Third relation

$$\begin{aligned}
 M_{ijkl}^{-1}(\varphi = 0) &= I_{ijkl} \\
 M_{1313}^{-1} &= \frac{1}{2}[(\delta_{11} - \varphi_{11})\delta_{33} + \delta_{11}(\delta_{33} - \varphi_{33})] = 0.5[(1 - \varphi_{11}) + (1 - \varphi_{33})] \\
 M_{1331}^{-1} &= \frac{1}{2}[(\delta_{13} - \varphi_{13})\delta_{31} + \delta_{13}(\delta_{31} - \varphi_{31})] = 0 \\
 &\Rightarrow M_{1313}^{-1} \neq M_{1331}^{-1}.
 \end{aligned}$$

2.2.4 Fourth relation

$$\begin{aligned}
 M_{ijkl}^{-1}(\varphi = 0) &= I_{ijkl}^s \\
 M_{1313} &= \frac{1}{2}[(\delta_{13} - \varphi_{13})^{-1}\delta_{13} + \delta_{13}(\delta_{13} - \varphi_{13})^{-1}] = 0 \\
 M_{1331} &= \frac{1}{2}[(\delta_{13} - \varphi_{13})^{-1}\delta_{31} + \delta_{11}(\delta_{33} - \varphi_{33})^{-1}] = 0.5(1 - \varphi_{33})^{-1} \\
 &\Rightarrow M_{1313} \neq M_{1331}.
 \end{aligned}$$

2.2.5 Utilized relation

$$\begin{aligned}
 M_{ijkl}^{-1}(\varphi = 0) &= I_{ijkl}^s \\
 M_{ijkl}^{-1} &= \frac{1}{4}[(\delta_{ik} - \varphi_{ik})\delta_{jl} + (\delta_{jl} - \varphi_{jl})\delta_{ik} + (\delta_{il} - \varphi_{il})\delta_{jk} + (\delta_{jk} - \varphi_{jk})\delta_{il}] \\
 M_{ijlk}^{-1} &= \frac{1}{4}[(\delta_{il} - \varphi_{il})\delta_{jk} + (\delta_{jk} - \varphi_{jk})\delta_{il} + (\delta_{ik} - \varphi_{ik})\delta_{jl} + (\delta_{jl} - \varphi_{jl})\delta_{ik}] \\
 M_{klij}^{-1} &= \frac{1}{4}[(\delta_{ki} - \varphi_{ki})\delta_{lj} + (\delta_{lj} - \varphi_{lj})\delta_{ki} + (\delta_{kj} - \varphi_{kj})\delta_{li} + (\delta_{li} - \varphi_{li})\delta_{kj}] \\
 &\Rightarrow M_{ijkl}^{-1} = M_{ijlk}^{-1} = M_{klij}^{-1}.
 \end{aligned}$$

The proposed relation can be expressed as a 6×6 matrix:

$$M_{ijkl}^{-1} = \begin{pmatrix} (1 - \varphi_{11}) & 0 & 0 & -\varphi_{12} & 0 & -\varphi_{13} \\ 0 & (1 - \varphi_{22}) & 0 & -\varphi_{21} & -\varphi_{23} & 0 \\ 0 & 0 & (1 - \varphi_{33}) & 0 & -\varphi_{32} & -\varphi_{31} \\ -\varphi_{12}/2 & -\varphi_{21}/2 & 0 & [(1 - \varphi_{11}) + (1 - \varphi_{22})]/2 & -\varphi_{13}/2 & -\varphi_{23}/2 \\ 0 & -\varphi_{23}/2 & -\varphi_{32}/2 & -\varphi_{13}/2 & [(1 - \varphi_{22}) + (1 - \varphi_{33})]/2 & -\varphi_{21}/2 \\ -\varphi_{13}/2 & 0 & -\varphi_{31}/2 & -\varphi_{23}/2 & -\varphi_{21}/2 & [(1 - \varphi_{11}) + (1 - \varphi_{33})]/2 \end{pmatrix}.$$

2.2.6 Discussion

When the damage process is not started, or the damage parameters are very close to zero, the nominal and effective stress in the material are expected to be equal. However, the above calculations show that the first and fifth damage effect tensors change the undamaged stress in the transition from effective to nominal configuration and turn the uniaxial experiment to an equi-triaxial test, which leads to unacceptable results. The second and fourth tensors are not equal (i.e., M_{1331} is different in second and fourth relations) and one may be hesitant about selecting them. Moreover, the second, third, and fourth damage effect tensors possess major symmetry but do not have minor symmetry property. Nevertheless, because of symmetry of the stress tensor, the asymmetry of the damage effect tensor may not affect the results of Eq. (1).

Hence, considering the deficiencies of available damage effect tensors, an improved relation is used in the ADPM of this paper, which guarantees both the minor and major symmetry properties.

2.3 Spectral decomposition of the stress tensor

Due to the existence of microcracks, the concrete is more brittle in tension, and the stiffness of damaged concrete differs for tensile and compressive loads. The change in material stiffness is due to the crack closing and reopening in transition from positive stress state, in direction perpendicular to crack surface, to negative stress state and vice versa. This distinct behavior in tension and compression is called the unilateral effect. Therefore, the stress tensor is decomposed into positive and negative parts, which perfectly consider concrete's unilateral effect:

$$\sigma_{ij} = \sigma_{ij}^+ + \sigma_{ij}^-, \quad \bar{\sigma}_{ij} = \bar{\sigma}_{ij}^+ + \bar{\sigma}_{ij}^- \quad (7)$$

Here, $\bar{\sigma}_{ij}^\pm$ is calculated as follows:

$$\begin{aligned} \bar{\sigma}_{kl}^+ &= P_{klpq}^+ \bar{\sigma}_{pq} \\ \bar{\sigma}_{kl}^- &= [I_{klpq} - P_{klpq}^+] \bar{\sigma}_{pq} = P_{klpq}^- \bar{\sigma}_{pq} \end{aligned} \quad (8)$$

where P_{klpq}^\pm is the set of stress projection tensors such that:

$$P_{klpq}^+ = \sum_{j=1}^3 H(\hat{\sigma}^{(j)}) n_k^{(j)} n_l^{(j)} n_p^{(j)} n_q^{(j)}, \quad P_{klpq}^- = I_{klpq} - P_{klpq}^+ \quad (9)$$

where $H(\hat{\sigma}^{(j)})$ is the Heaviside step function. This is equal to one if $\hat{\sigma}^{(j)} > 0$ and zero otherwise. Also, $n^{(j)}$ and $\hat{\sigma}^{(j)}$ are the j th eigenvector and eigenvalue of the stress tensor, respectively. For anisotropic damage, the inverse of the damage effect tensor is easily defined as:

$$M_{ijpq}^{-1} = M_{ijkl}^{-1+} P_{klpq}^+ + M_{ijkl}^{-1-} P_{klpq}^- \quad (10)$$

By multiplying $\bar{\sigma}_{ij}$ in both sides of Eq. (10) and using Eq. (1), the nominal stress tensor is obtained as follows:

$$\sigma_{ij} = M_{ijkl}^{-1+} P_{klpq}^+ \bar{\sigma}_{pq} + M_{ijkl}^{-1-} P_{klpq}^- \bar{\sigma}_{pq} = M_{ijkl}^{-1+} \bar{\sigma}_{kl}^+ + M_{ijkl}^{-1-} \bar{\sigma}_{kl}^- \quad (11)$$

where M_{ijkl}^{-1} in decomposed configuration ($M_{ijkl}^{-1\pm}$) is a function of positive/negative damage variable:

$$M_{ijkl}^{-1\pm} = \frac{1}{4} \left[(\delta_{ik} - \varphi_{ik}^\pm) \delta_{jl} + (\delta_{jl} - \varphi_{jl}^\pm) \delta_{ik} + (\delta_{il} - \varphi_{il}^\pm) \delta_{jk} + (\delta_{jk} - \varphi_{jk}^\pm) \delta_{il} \right] \quad (12)$$

Finally, it is worth mentioning that:

$$\begin{aligned} M_{ijkl}^{-1} &\neq M_{ijkl}^{-1+} + M_{ijkl}^{-1-} \\ \varphi_{ij} &\neq \varphi_{ij}^+ + \varphi_{ij}^- \end{aligned} \quad (13)$$

2.4 Plastic and damage yield surfaces

A stress-based yield criterion is employed here in the effective configuration to separate the elastic and plastic regions and define the onset of irreversible strains. Hence, the yield function, initially introduced by Lubliner et al. [29] and modified by Lee and Fenves [30], is adopted here. A non-associated flow rule is also used to describe the increment of plastic strain after yielding. Hence, two different functions are considered here for the yield criterion and the plastic potential functions, the parameters of which were derived from experimental tests.

$$f = \sqrt{3J_2} + \alpha\bar{I}_1 + \beta(\bar{\varepsilon}_{\text{eq}}^{\pm P})H(\hat{\sigma}_{\text{max}})\hat{\sigma}_{\text{max}} - (1 - \alpha)\bar{c}^-(\bar{\varepsilon}_{\text{eq}}^{-P}) = 0 \quad (14)$$

where \bar{I}_1 is the first invariant of the effective stress tensor, \bar{J}_2 is the second invariant of the deviatoric effective stress tensor, $\hat{\sigma}_{\text{max}}$ is the maximum principal effective stress, and $\bar{\varepsilon}_{\text{eq}}^{\pm P}$ is the equivalent plastic strain.

Because of the unilateral effect, the behavior of concrete is different in tension and compression in a uniaxial stress state. This can also be observed in a general stress state, where the behavior of concrete in every principal direction depends on whether the stress in that direction is positive or negative. Therefore, the yield criterion has to consider both distinct behaviors. Therefore, $H(\hat{\sigma}_{\text{max}})$ is used to separate tensile and compressive yield functions.

The parameters α and β can be calculated as follows:

$$\alpha = \frac{(f_{b0}/f_0^-) - 1}{2(f_{b0}/f_0^-) - 1}, \quad \beta = (1 - \alpha)\frac{\bar{c}^-(\bar{\varepsilon}_{\text{eq}}^{-P})}{\bar{c}^+(\bar{\varepsilon}_{\text{eq}}^{+P})} - (1 + \alpha) \quad (15)$$

where f_0^+ , f_0^- and f_{b0} are initial yield strengths under uniaxial tension and compression and biaxial compression, respectively. Furthermore, \bar{c}^{\pm} in Eq. (15) is the isotropic hardening function defined here by the following relations:

$$\bar{c}^- = f_0^- + Q\left[1 - \exp(-b\bar{\varepsilon}_{\text{eq}}^{-P})\right], \quad \bar{c}^+ = f_0^+ + h\bar{\varepsilon}_{\text{eq}}^{+P} \quad (16)$$

where Q , b and h are material constants, which can be determined from the material effective stress–strain diagram. The classic Drucker–Prager criterion is used here as the plastic potential function:

$$F^P = \sqrt{3J_2} + \alpha^P\bar{I}_1 \quad (17)$$

A non-associated plastic flow rule is employed here to properly define the volume expansion of concrete under compression. Hence, the plastic strain increment is defined as:

$$\dot{\varepsilon}_{ij}^p = \dot{\lambda}^P \frac{\partial F^P}{\partial \sigma_{ij}} \quad (18)$$

where $\dot{\lambda}^P$ is the plastic multiplier.

Two anisotropic damage functions in positive and negative configurations are employed here [54, 71]:

$$g^{\pm} = \sqrt{\frac{1}{2}Y_{ij}^{\pm}L_{ijkl}Y_{kl}^{\pm}} - K^{\pm}(\varphi_{\text{eq}}^{\pm}) \leq 0 \quad (19)$$

where Y_{ij}^{\pm} is the positive/negative damage driving force, which governs the damage criterion evolution and can be expressed by the following relation:

$$Y_{rs}^{\pm} = -\frac{1}{2}\bar{E}_{ijab}^{-1}\bar{\sigma}_{ab} \frac{\partial M_{ijpq}^{\pm-1}}{\partial \varphi_{rs}^{\pm}} \bar{\sigma}_{pq} \quad (20)$$

$K^{\pm}(\varphi_{\text{eq}}^{\pm})$ in Eq. (19) is the damage hardening function, $\varphi_{\text{eq}}^{\pm}$ is the equivalent damage parameter, and L_{ijkl} is a fourth-order tensor such that:

$$L_{ijkl} = 2\eta\delta_{ij}\delta_{kl} + (1 - \eta)(\delta_{ik}\delta_{jl} + \delta_{il}\delta_{jk}) \quad (21)$$

The evolution of anisotropic damage parameters is calculated using the damage flow rule:

$$\dot{\phi}_{ij}^{\pm} = \dot{\lambda}^{d^{\pm}} \frac{\partial g^{\pm}}{\partial Y_{ij}^{\pm}} \quad (22)$$

in which $\dot{\lambda}^{d^{\pm}}$ is the damage multiplier. $\varphi_{\text{eq}}^{\pm}$ in relation (19) is an accumulative scalar parameter introducing isotropic damage hardening, which is equal to:

$$\varphi_{\text{eq}}^{\pm} = \int_0^t |\dot{\varphi}_{\text{eq}}^{\pm}| dt \quad (23)$$

where the rate of equivalent damage variable is:

$$\dot{\varphi}_{\text{eq}}^{\pm} = \sqrt{\dot{\varphi}_{ij}^{\pm} \dot{\varphi}_{ij}^{\pm}} = \beta \dot{\lambda}^{d^{\pm}}, \quad \beta = \sqrt{\frac{L_{mnkl}^{\pm} Y_{kl}^{\pm} L_{mnpq}^{\pm} Y_{pq}^{\pm}}{2 Y_{ab}^{\pm} L_{abcd}^{\pm} Y_{cd}^{\pm}}}. \quad (24)$$

2.5 Damage hardening function

This subsection aims to compare the performance of two different alternatives for the damage hardening function in Eq. (19). The first alternative proposes the following exponential function for K^{\pm} , as used in many previous studies [54–57, 59, 66]:

$$K^{\pm} = K_0^{\pm} \left[1 - \frac{1}{B^{\pm}} \ln(1 - \varphi_{\text{eq}}^{\pm}) \right] \quad (25)$$

where K_0^{\pm} is the damage initiation threshold, which implies the area under the linear region of material stress–strain diagram, bounded by origin and f_0^{\pm} .

Considering Eq. (25), $\varphi_{\text{eq}}^{\pm}$ can be expressed as:

$$\begin{aligned} \varphi_{\text{eq}}^{-} &= 1 - \exp \left[B^{-} \left(1 - \frac{K^{-}}{K_0^{-}} \right) \right] \\ \varphi_{\text{eq}}^{+} &= 1 - \frac{K_0^{+}}{K^{+}} \exp \left[B^{+} \left(1 - \frac{K^{+}}{K_0^{+}} \right) \right] \end{aligned} \quad (26)$$

The term K_0^{+}/K^{+} is added in φ_{eq}^{+} to control the excessive damage growth in tensile loading. The evolution of damage hardening functions can be defined by taking the derivatives of Eq. (25):

$$\begin{aligned} \dot{K}^{-} &= \frac{K_0^{-}}{B^{-}} \exp \left[-B^{-} \left(1 - \frac{K^{-}}{K_0^{-}} \right) \right] \dot{\varphi}_{\text{eq}}^{-} \\ \dot{K}^{+} &= \frac{K^{+}}{B^{+} + \frac{K_0^{+}}{K^{+}}} \exp \left[-B^{+} \left(1 - \frac{K^{+}}{K_0^{+}} \right) \right] \dot{\varphi}_{\text{eq}}^{+} \end{aligned} \quad (27)$$

Considering Eq. (19), one can substitute K^{\pm} with $\sqrt{(1/2)Y_{ij}^{\pm}L_{ijkl}Y_{kl}^{\pm}}$ in the mentioned relations. Also, B^{\pm} is a material parameter which is defined as follows [2, 54, 67]:

$$B^{\pm} = \left[\frac{G_f^{\pm} \bar{E}}{l^* f_0^{\pm 2}} - \frac{1}{2} \right]^{-1} \geq 0 \quad (28)$$

where G_f^{\pm} is the fracture energy and l^* is the characteristic length scale determined as the cube root of the tributary volume at each Gauss point.

The second alternative for K^{\pm} is a power relation proposed by Abu Al-Rub and Kim [66]:

$$K^{\pm} = K_0^{\pm} \left[1 + \left(\frac{1}{B^{\pm}} \varphi_{\text{eq}}^{\pm} \right)^{q^{\pm}} \right] \quad (29)$$

where q^\pm is a material constant. Abu Al-Rub and Kim [66] compared the exponential and power relations and indicated that the results of the power relation, even by $q^\pm = 1$, agree better with experiments. The tensile equivalent damage variable is slightly modified here in order to obtain better predictions in multiaxial loadings:

$$\begin{aligned}\varphi_{\text{eq}}^+ &= B^+ \left(\frac{K_0^+ \times \alpha}{K^+} \right) \left(\frac{K^+}{K_0^+} - 1 \right)^{q^+}, \quad \alpha = \text{trace} \left(\frac{\partial g^+}{\partial Y^+} \right) \\ \varphi_{\text{eq}}^- &= B^- \left(\frac{K^-}{K_0^-} - 1 \right)^{q^-}\end{aligned}\quad (30)$$

Moreover, the evolution of damage hardening functions can be calculated by taking the derivatives of Eq. (29):

$$\begin{aligned}\dot{K}^+ &= \frac{K^+}{B^+ \left(q^+ - 1 + \frac{K_0^+}{K^+} \right)} \left[\frac{K^+}{K_0^+} - 1 \right]^{1-q^+} \dot{\varphi}_{\text{eq}}^+ \\ \dot{K}^- &= \frac{K_0^-}{B^- q^-} \left[\frac{K^-}{K_0^-} - 1 \right]^{1-q^-} \dot{\varphi}_{\text{eq}}^-\end{aligned}\quad (31)$$

2.5.1 Comparison

In order to evaluate the effectiveness of exponential and power damage hardening functions, the experimental test of Kupfer et al. [72] is numerically simulated, and the results of the mentioned formulations are compared and discussed here. Therefore, using the displacement control loading mode, an eight-node single element with eight Gauss integration points is monotonically subjected to uniaxial and biaxial compressive loading. Table 2 presents the material parameters. Figure 1 also shows the stress–strain and damage–strain curves of both alternatives. In uniaxial loading, the results show a good agreement with experimental data for both alternatives.

In contrast, the model using the exponential relation in biaxial loading cannot predict the experimental result, and the nominal stress deviates from the experimental curve in the softening region. To further clarify the mentioned deficiency, the presented alternatives are compared in larger amounts of equivalent damage. For this purpose, Q is increased to 150, and the biaxial test is performed again using the exponential and power relations. The nominal stress–strain and damage–strain diagrams are shown in Fig. 2. The damage results of each case, at the end of analysis, are also listed in Table 3.

The main reason for the disparity between the results is that the equivalent damage in Eq. (25) has a mathematical upper bound (i.e., $0 \leq \varphi_{\text{eq}}^\pm \leq 1$). Therefore, in an equi-biaxial loading in directions 1 and 2, the sum of damage squares in loading directions is limited to 1:

$$\begin{aligned}\dot{\varphi}_{\text{eq}} &= \sqrt{\dot{\varphi}_{11}^2 + \dot{\varphi}_{22}^2}, \quad \dot{\varphi}_{11} = \dot{\varphi}_{22} \\ 0 \leq \varphi_{\text{eq}} \leq 1 &\Rightarrow 0 \leq \varphi_{11}^2 + \varphi_{22}^2 \leq 1\end{aligned}\quad (32)$$

Thus, the damage parameters are bounded to 0.707 in every loading direction, which is physically meaningless. This is because, in an equi-biaxial loading, $(\partial g^\pm / \partial Y^\pm)_{11}$ and $(\partial g^\pm / \partial Y^\pm)_{22}$ in Eq. (22) are equal to 0.707.

For more clarification, consider a three-phase uniaxial test on a single element, in which the element is loaded in directions 1, 2, and 3, respectively. In the first phase φ_{eq} is increased to 0.8; therefore, φ_{11} reaches 0.8. Then in the second phase, φ_{eq} increases to its maximum value, forced by exponential relation, (i.e., 1), and consequently, φ_{22} reaches 0.2 (i.e., $0 \leq \varphi_{22} \leq 0.2$). In the third phase, the uniaxial loading continues in

Table 2 Material properties

ν	\bar{E} (MPa)	f_0^- (MPa)	Q (MPa)	b	K_0^-	B^-	q^-
0.2	29,000	15	70	810	0.013	0.2	0.7

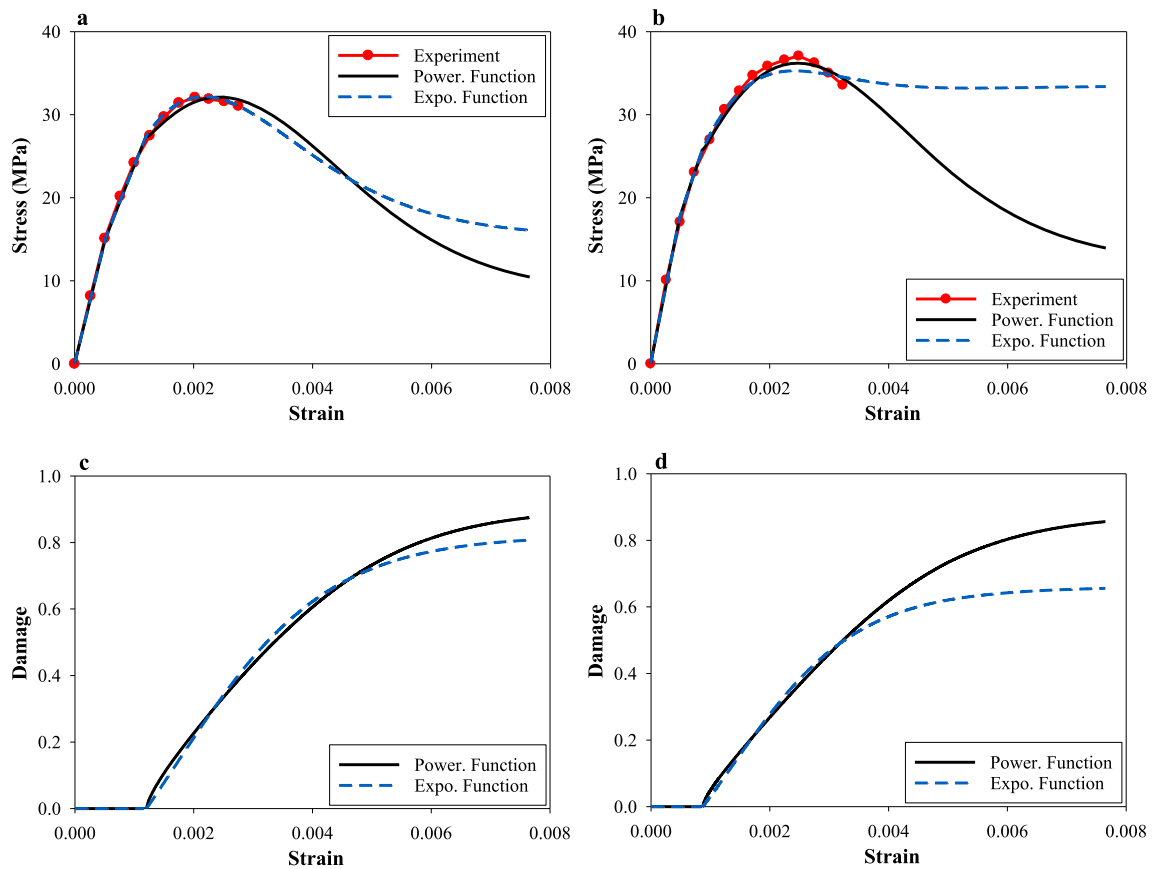


Fig. 1 Numerical results of uniaxial and biaxial tests compared with Kupfer et al. [72]: **a** uniaxial stress–strain curves, **b** biaxial stress–strain curves, **c** uniaxial damage–strain curve, **d** biaxial damage–strain curve

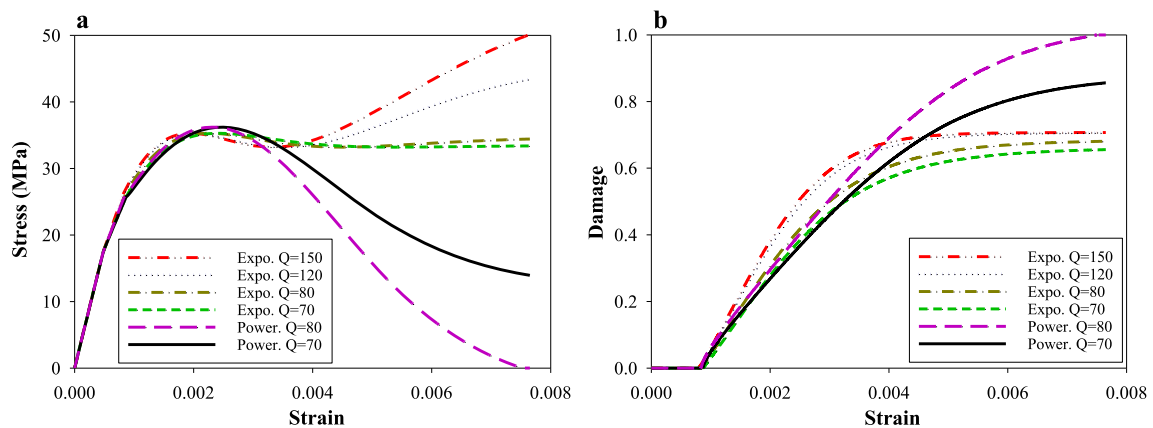


Fig. 2 The results of biaxial test with power and exponential damage laws for different amounts of Q ; **a** stress–strain curves, **b** damage–strain curves

direction 3, but as the equivalent damage has reached its upper bound, φ_{33} remains equal to zero. This damage freeze means that the damage growth in different orientations is not an independent procedure, which leads to discrepant results.

Furthermore, when φ_{eq} unrealistically reaches its upper bound in a biaxial test and all the damage parameters reach a constant value (i.e., 0.707), M^{-1} will therefore be a nonzero constant tensor. This means σ increases with $\bar{\sigma}$, which is in contrast to the decreasing stress in the softening region observed in experiments. This is

Table 3 The damage characteristics at the end of each test

Test no.	Damage hardening function	Q	φ_{eq}	φ_{ij}			$\partial g/\partial y$		
1	Exponential	70	0.927	0	0	0	0	0	0
				0	0.656	0	0	0.707	0
2	Exponential	80	0.963	0	0	0.656	0	0	0.707
				0	0.681	0	0	0.707	0
3	Exponential	120	0.998	0	0	0.681	0	0	0.707
				0	0.706	0	0	0.707	0
4	Exponential	150	1.000	0	0	0.706	0	0	0.707
				0	0.707	0	0	0.707	0
5	Power	70	1.211	0	0	0.707	0	0	0.707
				0	0.856	0	0	0.707	0
6	Power	80	1.419	0	0	0.856	0	0	0.707
				0	1.000	0	0	0.707	0
				0	0	1.000	0	0	0.707

shown in Fig. 2. Daneshyar and Ghaemian [59] also observed this artificial stiffness in the results of notched beam under cyclic loading.

In order to treat the deficiencies of exponential relation, the power relation is employed in the ADPM of present study. It is worth noting that φ_{eq} in the power relation (Eq. 29) has no mathematical upper bound and grows up to the point where all the components of damage tensor reach their respective physical upper bounds ($0 \leq \varphi_{eq}^{\pm}$, $0 \leq \varphi_{ij}^{\pm} \leq 1$).

The main findings of this subsection can be summarized as follows:

- Using exponential relation in multiaxial test: 1. results in physically unacceptable limits for damage parameters, 2. causes the damage tensor to freeze, 3. violates the damage parameter independency in different orientations, 4. yields artificial stiffness in stress–strain curve, and consequently leads to meaningless results.
- In the case of using power relation, the upper bound of damage parameters in loading directions is 1. Hence, mathematically, the equivalent damage is not a limiting parameter and increases until all damage parameters reach 1.
- The problems raised in exponential relation are observed in multiaxial loading tests.
- Mentioned problems get intensified by increasing Q .

2.6 Comparison of 3 alternatives for damage formulation

This subsection aims to evaluate the model performance with different combinations of available options for continuum damage relations (i.e., damage effect tensor and damage driving force). To this end, three options are considered and compared here for the formulation of the damage model. These proposed alternatives are listed in Table 4.

It is worth mentioning that the second method is proposed by Abu Al-Rub and Kim [66]. The monotonic uniaxial and biaxial compressive test of Kupfer et al. [72] is adopted to compare the performance of presented alternatives. For this purpose, a single element is subjected to a monotonic uniaxial and equi-biaxial (i.e., $\varepsilon_1 = \varepsilon_2$) compression through the displacement control loading mode. The utilized material properties are presented in Table 5. The difference in damage constants is because of the difference in damage formulation of the different alternatives. The material constants are the same in both uniaxial and biaxial tests. Figure 3 shows the numerical results generated by different alternatives along with the experimental curve. In the uniaxial test, the results of all options show a perfect agreement with experimental data. In contrast, in the biaxial test, the first and second options fail to predict the material response. The third method, nevertheless, successfully predicts the test results in both uniaxial and biaxial loading states. Hence, the third alternative is adopted for the damage formulation of the proposed ADPM model.

Table 4 Proposed alternatives for the formulation of the damage model

Alternative	Details
1	$Y_{ij}^{\pm} = \bar{\sigma}_{ij}^{\pm}, K^{\pm} = K_0^{\pm} \left[1 + \left(\varphi_{\text{eq}}^{\pm} / B^{\pm} \right)^{1/q^{\pm}} \right]$ $M_{ijkl}^{-1} = \frac{1}{2} [(\delta_{im} - \varphi_{im})(\delta_{jm} - \varphi_{jm})\delta_{kl} + \delta_{ij}(\delta_{km} - \varphi_{km})(\delta_{lm} - \varphi_{lm})]$ Damage hardening parameter: Method 3*
2	$Y_{rs}^{\pm} = -\frac{1}{2} \bar{E}_{ijab}^{-1} \bar{\sigma}_{ab} \frac{\partial M_{ijpq}^{\pm}}{\partial \varphi_{rs}^{\pm}} \bar{\sigma}_{pq}, K^{\pm} = K_0^{\pm} \left[1 + \left(\varphi_{\text{eq}}^{\pm} / B^{\pm} \right)^{1/q^{\pm}} \right]$ $M_{ijkl}^{-1} = \frac{1}{2} [(\delta_{im} - \varphi_{im})(\delta_{jm} - \varphi_{jm})\delta_{kl} + \delta_{ij}(\delta_{km} - \varphi_{km})(\delta_{lm} - \varphi_{lm})]$ Damage hardening parameter: Method 1*
3	$Y_{rs}^{\pm} = -\frac{1}{2} \bar{E}_{ijab}^{-1} \bar{\sigma}_{ab} \frac{\partial M_{ijpq}^{\pm}}{\partial \varphi_{rs}^{\pm}} \bar{\sigma}_{pq}, K^{\pm} = K_0^{\pm} \left[1 + \left(\varphi_{\text{eq}}^{\pm} / B^{\pm} \right)^{1/q^{\pm}} \right]$ $M_{ijkl}^{-1} = \frac{1}{4} [(\delta_{ik} - \varphi_{ik})\delta_{jl} + (\delta_{jl} - \varphi_{jl})\delta_{ik} + (\delta_{il} - \varphi_{il})\delta_{jk} + (\delta_{jk} - \varphi_{jk})\delta_{il}]$ Damage hardening parameter: Method 3*

*Damage hardening parameter calculation methods are described in sub-Sect. 3.4

Table 5 Material properties

Alternative	ν	\bar{E} (MPa)	f_0^- (MPa)	Q (MPa)	b	K_0^-	B^-	q^-
1	0.2	29,000	15	70	810	22.5	0.16	1.29
2	0.2	29,000	15	70	810	0.02	0.055	1.4
3	0.2	29,000	15	70	810	0.013	0.2	0.7

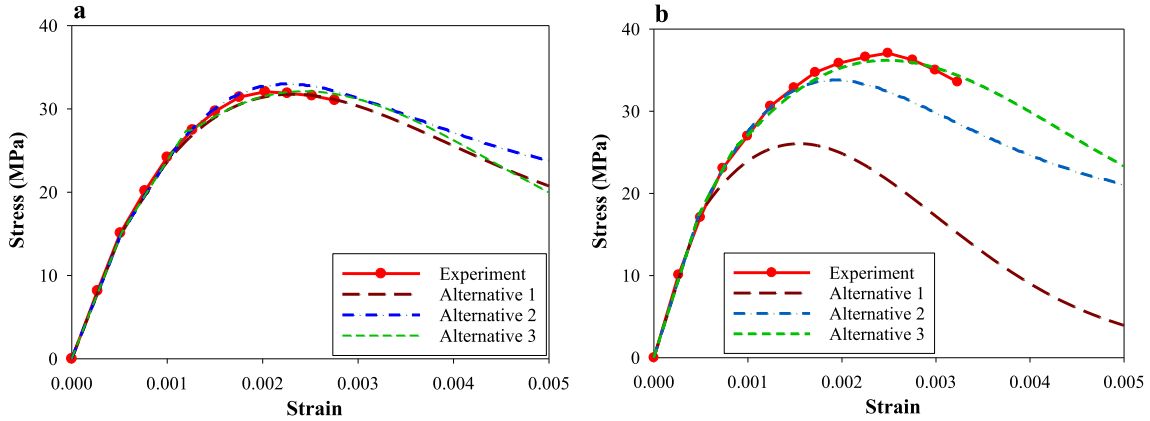


Fig. 3 Comparison of stress–strain curves of three proposed alternatives with compressive test of Kupfer et al. [72]: **a** uniaxial loading, **b** biaxial loading

3 Numerical implementation

There are two methods in the literature for stress updating in an ADPM model: the coupled formulation for the anisotropic damage and plasticity [55, 56] and the decoupled approach [54, 66]. Zhu et al. [73] compared the coupled and decoupled approaches with isotropic damage and found that the decoupled algorithm provides better convergence and a satisfactory numerical accuracy. Hence, the decoupled method is adopted in this study. In this regard, a two-step algorithm is used which, in the first step, updates the effective stress and, in the second step, updates the damage tensor and the nominal stress.

In the first step, a conventional return mapping algorithm is adopted, in which $\bar{\sigma}$ and $\boldsymbol{\varepsilon}^p$ are updated using an elastic predictor plastic corrector method. Accordingly, the trial effective stress, at step $n + 1$, is updated as follows:

$$\bar{\sigma}_{n+1}^{\text{tr}} = E_0(\boldsymbol{\varepsilon}_{n+1} - \boldsymbol{\varepsilon}_n^p) \quad (33)$$

If the trial stress locates beyond the yield surface (i.e., $F(\bar{\sigma}_{n+1}^{tr}, \bar{\varepsilon}_{eq,n}^{\pm p}) > 0$), it should be updated in an iterative approach to determine a new admissible state. The consistency condition is also used to guarantee that the predicted stress lies on the yield surface at the end of the plastic step.

$$\text{if } F(\bar{\sigma}_{n+1}^{tr}, \bar{\varepsilon}_{eq,n}^{\pm p}) > 0 \text{ then } \bar{\sigma}_{n+1} = \bar{\sigma}_{n+1}^{tr} - E_0 \Delta \boldsymbol{\varepsilon}^p = \bar{\sigma}_n + \Delta \bar{\boldsymbol{\sigma}}^e - E_0 \Delta \lambda^p \frac{\partial F^p}{\partial \bar{\boldsymbol{\sigma}}} \quad (34)$$

In the damage step, the transformation of the effective stress to the nominal stress is performed in accordance with the history of damage. The decomposition of effective stress tensor into positive and negative parts is performed at the beginning of the damage step. Hence, two damage criteria, two damage tensors, and two damage effect tensors are adopted for positive and negative stress states.

The damage criterion is used to determine the damage yielding condition for effective stress state so that if $g^+ > 0$ or $g^- > 0$, it is inferred that the tensile or compressive damage evolution has occurred in the material. Therefore, the damage tensor and the inverse of damage effect tensor must be updated using the effective stress of the current step and the damage tensor of the previous step. In contrast, $g^+ \leq 0$ or $g^- \leq 0$ show no growth in the material damage. Finally, the updated nominal stress, at the end of the damage step, is used to calculate the unbalanced force vector in the nonlinear analysis.

It is worth noting that in order to expedite the convergence rate in global iterations of the Newton–Raphson technique, the stiffness matrix of all elements must be updated in each iteration.

3.1 Continuum large cracking modification

In the classic plastic damage models, under tensile loading, by increasing the deformations and, subsequently, the strains in material, the elastic and plastic strains increase continuously, which leads to meaningless predictions. In brittle materials like concrete, the microcracks coalesce and form a macrocrack after an adequately large deformation. At this point, the material's behavior is similar to a discrete large crack, and the irreversible part of deformation remains constant by increasing the total deformation. Hence, in the numerical formulation, the evolution of irreversible tensile deformations (i.e., plastic strains) must be stopped at a distinct level of tensile damage. Accordingly, in the present study, the evolution of plastic strain is stopped if $\varphi_{n+1}^{eq} \geq \varphi_{cr}$, where φ_{cr} is the large crack threshold. In this regard, the plastic strain rate can be expressed as:

$$\dot{\boldsymbol{\varepsilon}}^p = (1 - r) \dot{\tilde{\boldsymbol{\varepsilon}}}^p \quad (35)$$

where $\tilde{\boldsymbol{\varepsilon}}^p$ and $\tilde{\boldsymbol{\sigma}}$ are intermediate plastic strain and intermediate effective stress, respectively. Moreover, the scalar variable $r = r(\hat{\tilde{\boldsymbol{\sigma}}})$ is a weight function (i.e., $0 \leq r \leq 1$)

$$r(\hat{\tilde{\boldsymbol{\sigma}}}) = \left(\sum_{i=1}^3 \langle \hat{\tilde{\sigma}}_i \rangle \right) / \left(\sum_{i=1}^3 |\hat{\tilde{\sigma}}_i| \right) \quad (36)$$

where $\tilde{\boldsymbol{\sigma}}$ at step $n + 1$ is equal to:

$$\tilde{\boldsymbol{\sigma}}_{n+1} = E_0 (\tilde{\boldsymbol{\varepsilon}}_{n+1} - \tilde{\boldsymbol{\varepsilon}}_{n+1}^p) \quad (37)$$

where

$$\tilde{\boldsymbol{\varepsilon}}_{n+1} = (1 - D_n^{cr}) \boldsymbol{\varepsilon}_{n+1} \quad (38)$$

The variable D^{cr} is introduced to make the evaluated intermediate effective stress in Eq. (37) return back onto the yield surface, such that (In the following κ^\pm is used instead of $\bar{\varepsilon}_{eq}^{\pm p}$ for simplicity):

$$F((1 - D^{cr}) \bar{\boldsymbol{\sigma}}, \boldsymbol{\kappa}) = 0 \quad (39)$$

Therefore, D^{cr} is expressed as:

$$D_{n+1}^{cr} = \max \left\{ D_n^{cr}, 1 - \frac{c_c (\bar{\varepsilon}^{-ep})}{f(\bar{\boldsymbol{\sigma}}_{n+1}, \boldsymbol{\kappa})} \right\} \quad (40)$$

The inverse of damage effect tensor is redefined considering large crack modification as follows:

$$\boldsymbol{M}^{-1} = (1 - D^{cr}) \boldsymbol{M}^{-1} \quad (41)$$

Figure 4 describes the algorithm for updating the effective and nominal stresses, adjusted for large cracking.

$$\begin{aligned}
& 0. \boldsymbol{\varepsilon}_{n+1}, \boldsymbol{\varepsilon}_n^p, \tilde{\boldsymbol{\varepsilon}}_n^p, \boldsymbol{\kappa}_n, \varphi_{ij,n}, D_n^{cr} \\
& 1. \bar{\boldsymbol{\sigma}}_{n+1}^{ir} = \mathbf{E}_0 : (\boldsymbol{\varepsilon}_{n+1} - \boldsymbol{\varepsilon}_n^p) \\
& 2. \tilde{\boldsymbol{\sigma}}_{n+1}^{ir} = (1 - D_n^{cr}) \bar{\boldsymbol{\sigma}}_{n+1}^{ir}, \quad \Delta \tilde{\boldsymbol{\sigma}}^e = (1 - D_n^{cr}) \Delta \bar{\boldsymbol{\sigma}}^e \\
& 3. F(\tilde{\boldsymbol{\sigma}}_{n+1}^{ir}, \boldsymbol{\kappa}_n) = f(\tilde{\boldsymbol{\sigma}}_{n+1}^{ir}, \boldsymbol{\kappa}_n) - c_c(\boldsymbol{\kappa}_n) \\
& 4. \text{IF } F(\tilde{\boldsymbol{\sigma}}_{n+1}^{ir}, \boldsymbol{\kappa}_n) \leq 0 \text{ THEN (Elastic loading/unloading state)} \\
& \quad 4.1. \bar{\boldsymbol{\sigma}}_{n+1} = \tilde{\boldsymbol{\sigma}}_{n+1}^{ir}; \boldsymbol{\varepsilon}_{n+1}^p = \boldsymbol{\varepsilon}_n^p; \tilde{\boldsymbol{\varepsilon}}_{n+1}^p = \tilde{\boldsymbol{\varepsilon}}_n^p; \boldsymbol{\kappa}_{n+1} = \boldsymbol{\kappa}_n; \varphi_{ij,n+1} = \varphi_{ij,n}; D_{n+1}^{cr} = D_n^{cr} \\
& 5. \text{ELSE (Plastic loading state)} \\
& \quad 5.1 \text{ Return-mapping process (local iteration to compute } \tilde{\boldsymbol{\sigma}}_{n+1}, \boldsymbol{\kappa}_{n+1}, \Delta \lambda^p) \\
& \quad \quad 5.1.1 \Delta \tilde{\boldsymbol{\varepsilon}}^p = \Delta \lambda^p \nabla_{\boldsymbol{\sigma}} F^p, \quad \tilde{\boldsymbol{\sigma}}_{n+1} = \tilde{\boldsymbol{\sigma}}_n + \Delta \tilde{\boldsymbol{\sigma}}^e - \mathbf{E}_0 \Delta \tilde{\boldsymbol{\varepsilon}}^p \\
& \quad \quad 5.1.2 \boldsymbol{\kappa}_{n+1} = \boldsymbol{\kappa}_n + \Delta \lambda^p \mathbf{H}(\hat{\boldsymbol{\sigma}}_{n+1}, \boldsymbol{\kappa}_{n+1}) \\
& \quad 5.2 \tilde{\boldsymbol{\varepsilon}}_{n+1}^p = \tilde{\boldsymbol{\varepsilon}}_n^p + \Delta \tilde{\boldsymbol{\varepsilon}}^p \\
& \quad 5.3 \text{IF } \varphi_{n+1}^{eq} < \varphi_{cr} \text{ THEN (Usual crack opening/closing state)} \\
& \quad \quad 5.3.1. \bar{\boldsymbol{\sigma}}_{n+1} = \tilde{\boldsymbol{\sigma}}_{n+1}; \boldsymbol{\varepsilon}_{n+1}^p = \tilde{\boldsymbol{\varepsilon}}_{n+1}^p; \Delta \boldsymbol{\varepsilon}^p = \Delta \tilde{\boldsymbol{\varepsilon}}^p; D_{n+1}^{cr} = \mathbf{0} \\
& \quad 5.4 \text{ELSE (Large crack opening/closing state)} \\
& \quad \quad 5.4.1. r_{n+1} = r(\tilde{\boldsymbol{\sigma}}_{n+1}) \\
& \quad \quad 5.4.2. \Delta \boldsymbol{\varepsilon}^p = (1 - r_{n+1}) \Delta \tilde{\boldsymbol{\varepsilon}}^p \\
& \quad \quad 5.4.3. \boldsymbol{\varepsilon}_{n+1}^p = \boldsymbol{\varepsilon}_n^p + \Delta \boldsymbol{\varepsilon}^p, \quad \bar{\boldsymbol{\sigma}}_{n+1} = \bar{\boldsymbol{\sigma}}_{n+1}^{ir} - \mathbf{E}_0 : \Delta \boldsymbol{\varepsilon}^p \\
& \quad \quad 5.4.4. D_{n+1}^{cr} = \max \left\{ D_n^{cr}, 1 - \frac{c_c(\bar{\boldsymbol{\varepsilon}}_{n+1}^p)}{f(\bar{\boldsymbol{\sigma}}_{n+1}, \boldsymbol{\kappa})} \right\} \\
& 6. \mathbf{M}^{-1} = (1 - D_{n+1}^{cr}) \mathbf{M}^{-1} \\
& 7. \boldsymbol{\sigma}_{n+1} = \mathbf{M}^{-1} \bar{\boldsymbol{\sigma}}_{n+1}
\end{aligned}$$

Fig. 4 The stress update algorithm with large cracking modification for an integration point

3.2 Viscoplastic formulation

Concrete behavior under cyclic loading is highly dependent on the loading rate. Consequently, when using rate-independent constitutive laws to simulate post-peak softening and stiffness degradation of concrete, convergence issues may arise and the model's response will be dependent on mesh and time increment. Hence, the uniqueness of the response is not guaranteed. On the other hand, using rate-dependent extension of the model can partially overcome the aforementioned numerical stability problems. Employing viscoplastic regularization improves the rate of convergence of the model [74] and reduces the dependency on mesh refinement and alignment [30]. The Duvaut–Lions model is employed here, whereby the plastic strain, effective stress, and equivalent damage variables are regularized to incorporate viscosity. Therefore, the evolution of viscoplastic strain tensor $\boldsymbol{\varepsilon}^{vp}$ is expressed as follows:

$$\dot{\boldsymbol{\varepsilon}}^{vp} = \frac{1}{\mu} (\boldsymbol{\varepsilon}^p - \boldsymbol{\varepsilon}^{vp}) \quad (42)$$

where μ is the viscosity parameter and represents the relaxation time of the viscoplastic model. The finite increment of viscous strain tensor is calculated through Eq. (42):

$$\Delta \boldsymbol{\varepsilon}^{vp} = (1 - \alpha_\mu) (\boldsymbol{\varepsilon}_{n+1}^p - \boldsymbol{\varepsilon}_n^{vp}) \quad (43)$$

where α_μ is the interpolation factor:

$$\alpha_\mu = \frac{\mu / \Delta t}{1 + \mu / \Delta t} \quad (44)$$

where Δt is the characteristic time increment. As $\boldsymbol{\varepsilon}_{n+1}^{vp} = \boldsymbol{\varepsilon}_n^{vp} + \Delta \boldsymbol{\varepsilon}^{vp}$, one can obtain the following relation for viscoplastic strain tensor:

$$\boldsymbol{\varepsilon}_{n+1}^{vp} = (1 - \alpha_\mu) \boldsymbol{\varepsilon}_{n+1}^p + \alpha_\mu \boldsymbol{\varepsilon}_n^{vp} \quad (45)$$

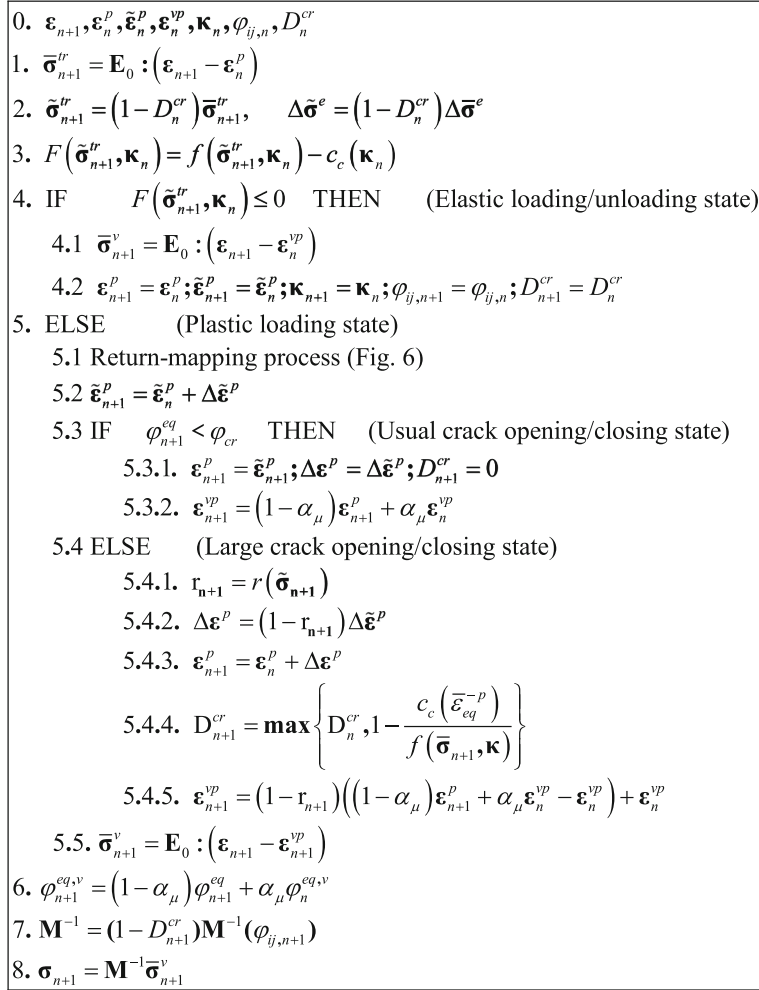


Fig. 5 The stress update algorithm at each integration point with large cracking and rate-dependency modifications

Additionally, the updated viscous equivalent damage variable can be calculated as follows:

$$\varphi_{n+1}^{eq,v} = (1 - \alpha_\mu) \varphi_{n+1}^{eq} + \alpha_\mu \varphi_n^{eq,v} \quad (46)$$

Figure 5 describes the implemented algorithm to update effective and nominal stress at each integration point, adjusted for large cracking and rate dependency.

3.3 Plastic hardening parameters

The tensile and compressive plastic hardening parameters can be expressed similar to Eq. (23):

$$\boldsymbol{\kappa} = \begin{pmatrix} \kappa^+ \\ \kappa^- \end{pmatrix}, \quad \kappa^\pm = \int_0^t \dot{\kappa}^\pm dt \quad (47)$$

where the rate of $\boldsymbol{\kappa}$ is defined as:

$$\dot{\boldsymbol{\kappa}} = \mathbf{h}(\hat{\boldsymbol{\sigma}}, \boldsymbol{\kappa}) : \hat{\boldsymbol{\varepsilon}}^p = \dot{\lambda}^p \mathbf{h} : \frac{\partial F^p}{\partial \hat{\boldsymbol{\sigma}}}, \quad \mathbf{h} = \begin{pmatrix} r(\hat{\boldsymbol{\sigma}}_{ij}) & 0 \\ 0 & -(1 - r(\hat{\boldsymbol{\sigma}}_{ij})) \end{pmatrix} \quad (48)$$

0. $j = 0$; $\hat{\sigma}_{n+1} = \hat{\sigma}_{n+1}^r$; $\kappa_{n+1}^{(0)} = \kappa_n$ 1. estimate $\Delta\lambda^P$ 2. estimate $\hat{\sigma}_{n+1}^j$ 3. $\mathbf{Q}_{n+1}^j = -\kappa_{n+1}^j + \kappa_n + \Delta\lambda^P \mathbf{H}(\hat{\sigma}_{n+1}^j, \kappa_{n+1}^j)$ 4. IF $\ \mathbf{Q}_{n+1}^j\ \leq TOL$ THEN Exit. 5. Solve $\left(\frac{d\mathbf{Q}}{d\kappa}\right)_{n+1}^j \Delta\kappa = -\mathbf{Q}(\kappa_{n+1}^j)$ for $\Delta\kappa$ 6. $\kappa_{n+1}^{j+1} = \kappa_{n+1}^j + \Delta\kappa$ 7. $j = j + 1$ and GOTO Step 1.

Fig. 6 The Iterative algorithm for the calculation of hardening parameters

Lee and Fenves [75] presented a formulation for the calculation of κ^\pm . They rewrote Eq. (48) in a discrete form as follows:

$$\kappa_{n+1} = \kappa_n + \Delta\lambda^P \mathbf{H}(\hat{\sigma}_{n+1}, \kappa_{n+1}) \quad (49)$$

Since Eq. (49) is a nonlinear function of κ , the calculation of κ_{n+1} , $\hat{\sigma}_{n+1}$ and $\dot{\lambda}^P$ requires an iterative solution (referred to as local iteration). For this purpose, the Newton–Raphson procedure is used in this paper. The residual of Eq. (49) can be defined as follows:

$$Q(\kappa_{n+1}, \hat{\sigma}_{n+1}, \dot{\lambda}^P) = -\kappa_{n+1} + \kappa_n + \Delta\lambda^P \mathbf{H}(\hat{\sigma}_{n+1}, \kappa_{n+1}) \quad (50)$$

The algorithm estimates κ_{n+1} in every iteration:

$$\kappa_{n+1}^{j+1} = \kappa_{n+1}^j + \Delta\kappa \quad (51)$$

The overview of the used local iteration algorithm is presented in Fig. 6:

3.4 Damage hardening parameters

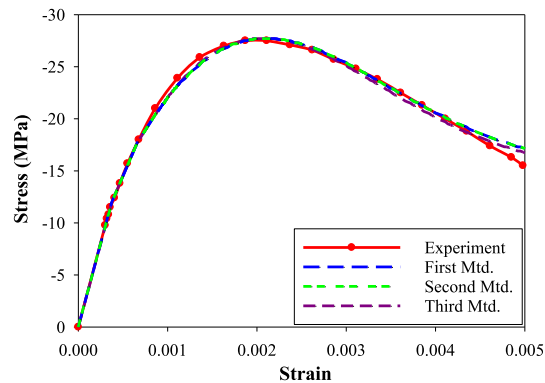
In order to determine the damage effect tensor, one needs to calculate the damage tensors and equivalent damage parameters. The damage hardening parameters φ_{eq}^\pm have to be calculated so that the tensile and compressive damage driving forces Y_{ij}^\pm remain on the damage surface in Eq. (19). This is very similar to calculation of plastic hardening parameters $\bar{\varepsilon}_{\text{eq}}^{\pm P}$ in Eq. (14). In the damage part, the damage yield criterion is used to recognize the damage initiation and growth, such that $g^\pm \geq 0$ shows the tensile/compressive damage growth in the material. Hence, one needs to employ a computationally efficient algorithm to obtain damage hardening parameters. Some studies in the literature propose an iterative method similar to the algorithm used to calculate the plastic hardening parameters. However, a different approach is proposed here, which is more efficient in terms of computational cost. In the following, three different methods, including the proposed method in this study and those in the literature, are described and compared:

3.4.1 Method 1

In the first method, the damage tensors can be obtained once the damage multipliers $\dot{\lambda}^{d^\pm}$ are calculated through the damage consistency condition [54–57, 66]. In this respect, Eqs. (22) and (24) can be used to obtain positive and negative damage tensors and equivalent damage parameters, respectively. However, since $\dot{\lambda}^{d^\pm}$ is a function of φ_{eq}^\pm and φ_{ij}^\pm , an iterative solution is needed to calculate $\dot{\lambda}^{d^\pm}$. A cumbersome iterative solution is required since the damage strain energy release rate Y_{ij}^\pm is a function of the fourth-order damage effect tensor M_{ijkl}^\pm [59]. Therefore, a local iteration is presented here to determine φ_{eq}^\pm , φ_{ij}^\pm and $\dot{\lambda}^{d^\pm}$ in the first method.

Table 6 Material properties

ν	\bar{E} (MPa)	f_0^- (MPa)	Q (MPa)	b	K_0^-	B^-	q^-
0.2	32,000	12	55.5	1100	0.005	0.105	0.78

**Fig. 7** Comparison of predicted stress–strain curves of three presented methods, based on uniaxial compressive test of Karsan and Jirsa [76]

3.4.2 Method 2

Similar to the first method, the damage multiplier has to be determined here to calculate the damage parameters using Eqs. (22) and (24). The significant difference is that in the second method, $\dot{\lambda}^{d\pm}$ is updated using φ_{eq}^{\pm} and φ_{ij}^{\pm} of the previous step, and no iterative procedure is used.

3.4.3 Method 3

The first method tries to determine $\dot{\lambda}^{d\pm}$ in an iterative procedure. This is similar to the return mapping algorithm used to determine $\dot{\lambda}^{p\pm}$ and $\bar{\sigma}_{ij}^{\pm}$ in the plasticity part. However, there is an important difference between the plasticity and damage parts of the decoupled solution proposed in this paper. In the local iteration used in the plasticity part, $\bar{\varepsilon}_{eq}^{\pm p}$ and $\bar{\sigma}_{ij}^{\pm}$ are updated simultaneously in every iteration. In contrast, in the damage yield criterion, $\bar{\sigma}_{ij}^{\pm}$ and, consequently, Y_{ij}^{\pm} are constant and only the damage hardening parameters have to be updated. Hence, one may directly use the damage function to update φ_{eq}^{\pm} without iteration. Therefore, in this method, the equivalent damage parameters are determined using Eq. (30). The main advantage of this approach is that the time-consuming iterative solution and the cumbersome calculation procedure of $\dot{\lambda}^{d\pm}$ are avoided.

3.4.4 Comparison

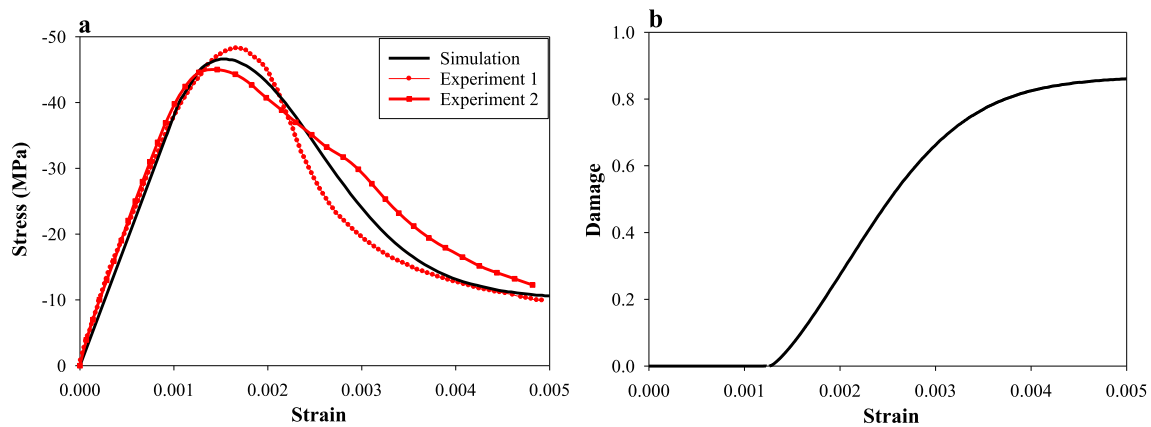
In order to compare the performance of the considered methods, the monotonic uniaxial compressive test of Karsan and Jirsa [76] is adopted here. In this test, a single element is subjected to monotonic compression through a displacement control loading mode. The properties of concrete material are presented in Table 6. Figure 7 shows the nominal stress–strain curves, predicted by the proposed methods, along with the experimental curve. All three methods are completely successful in predicting the material's response, and their results are in close agreement with the experimental data. The main difference between these methods is in their execution time. The execution time of the first, second and third methods is 01':58'', 00':45'' and 00':16'', respectively. This shows that the third method decreases the computational cost by 637% compared to the first method and guarantees higher convergence rate. Hence, the first and second methods are not cost-effective. It is essential to point out that in a nonlinear analysis with a complicated model consisting of hundreds of elements under a dynamic load (with hundreds of time steps), this execution time may be more significant.

Table 7 Material properties used for the compressive test of Zhang [77]

ν	\bar{E} (MPa)	f_0^- (MPa)	Q (MPa)	b	K_0^-	B^-	q^-
0.2	38,000	40	36	1800	0.0265	0.4	1.24

Table 8 Material properties used for the tensile test of Zhang [77]

ν	\bar{E} (MPa)	f_0^+ (MPa)	h	K_0^+	B^+	q^+
0.2	34,000	3.39	4500	0.00017	2.1	0.47

**Fig. 8** Numerical results of monotonic uniaxial compression compared with Zhang [77]: **a** stress–strain curves, **b** numerical damage–strain curve (in loading direction)

4 Experimental validation

The ADPM model is developed and implemented in an in-house finite element program, whereby the performance of the model is evaluated. The verification is performed first using four single-element experimental tests, including both monotonic and cyclic forms of compressive and tensile tests, followed by a full cyclic test. Next, the model is examined by three structural tests, including four-point bending and shear tests and an L-shaped concrete panel. For each case, the material parameters are presented.

4.1 Single-element tests

The verification of single-element tests is presented in the following. In all tests of this subsection, a 3D eight-node element with eight Gauss integration points is analyzed using the displacement control loading mode. Given the simplicity of mesh and loading for these tests, they are implemented in a rate-independent mode.

4.1.1 Monotonic uniaxial compressive and tensile tests

In order to examine the model's capabilities under compressive and tensile loadings, the monotonic uniaxial compressive and tensile tests of Zhang [77] are adopted here. The material properties of the single elements are listed in Tables 7 and 8. The effective stress–strain, nominal stress–strain, and damage–strain curves are illustrated in Fig. 8 for compressive and Fig. 9 for tensile test. The predicted results are in good agreement with the experimental data and perfectly demonstrate the softening behavior of concrete.

4.1.2 Cyclic uniaxial compressive and tensile tests

The compressive test of Karsan and Jirsa [76] and the tensile test of Taylor [78] are employed to assess the proposed model under cyclic loadings. In this regard, the single element undergoes uniaxial cyclic compressive/tensile loading. The material properties of concrete specimens are listed in Tables 9 and 10. The cyclic

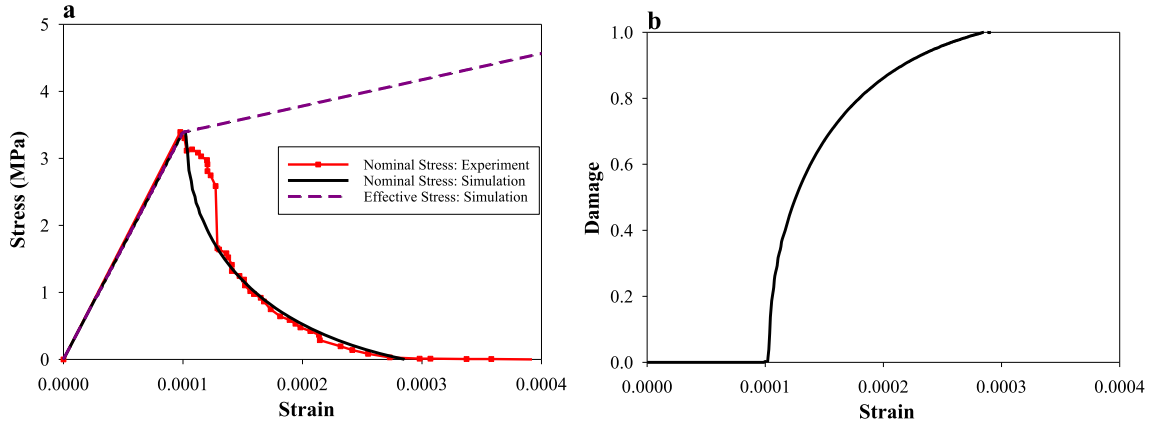


Fig. 9 Numerical results of monotonic uniaxial tensile test compared with Zhang [77]: **a** Stress–strain curves, **b** numerical damage–strain curve

Table 9 Material properties used for the compressive test of Karsan and Jirsa [76]

ν	\bar{E} (MPa)	f_0^- (MPa)	Q (MPa)	b	K_0^-	B^-	q^-
0.2	31,000	15	66	820	0.009	0.2	0.67

Table 10 Material properties used for the tensile test of Taylor [78]

ν	\bar{E} (MPa)	f_0^+ (MPa)	h	K_0^+	B^+	q^+
0.2	31,000	3.4	1500	0.000188	1.88	0.41

nominal stress–strain curves and the damage evolution diagram are plotted in Fig. 10 for compressive and Fig. 11 for tensile test. The results perfectly illustrate the ability of the model to simulate the reduction of unloading stiffness and irreversible deformations.

4.1.3 Full cyclic loading

A full cyclic uniaxial test is simulated through displacement control mode to evaluate the performance of the model under full cyclic loading. In this regard, the prescribed strain is defined in a way that the damage increases and the element undergoes nonlinear deformation in every positive and negative loading state.

The main goal of this test is to investigate the element’s response to the change in the load state from tensile to compressive and vice versa. Moreover, in this test, the rate dependency and large cracking are activated. Hence, three values of $\mu/\Delta t$ equal to 0, 1, and 3 are considered to show the influence of viscosity. Furthermore, the large cracking is started after φ^{eq} reaches 0.9 (i.e., $\varphi_{cr} = 0.9$). Figure 12 shows the stress–strain diagram of the element with three full loading cycles. This diagram shows an independent behavior in the tensile and compressive zones. Furthermore, the result indicates that after the elastic unloading process, by changing the load status from tension to compression, the tensile damage deactivates as the tensile cracks close and, as expected, the stiffness recovery is realized. The curves’ differences in softening and hardening regions demonstrate the effect of rate dependency on the element response. The results clearly show the effectiveness of the model in addressing irreversible deformations, stiffness degradation, and large cracking.

4.2 Structural validations

4.2.1 Four-point bending test

A simply supported concrete beam with a single notch under monotonic four-point loading is simulated to study the model’s performance in mode-I fracture. The beam is discretized with eight-node brick elements with eight

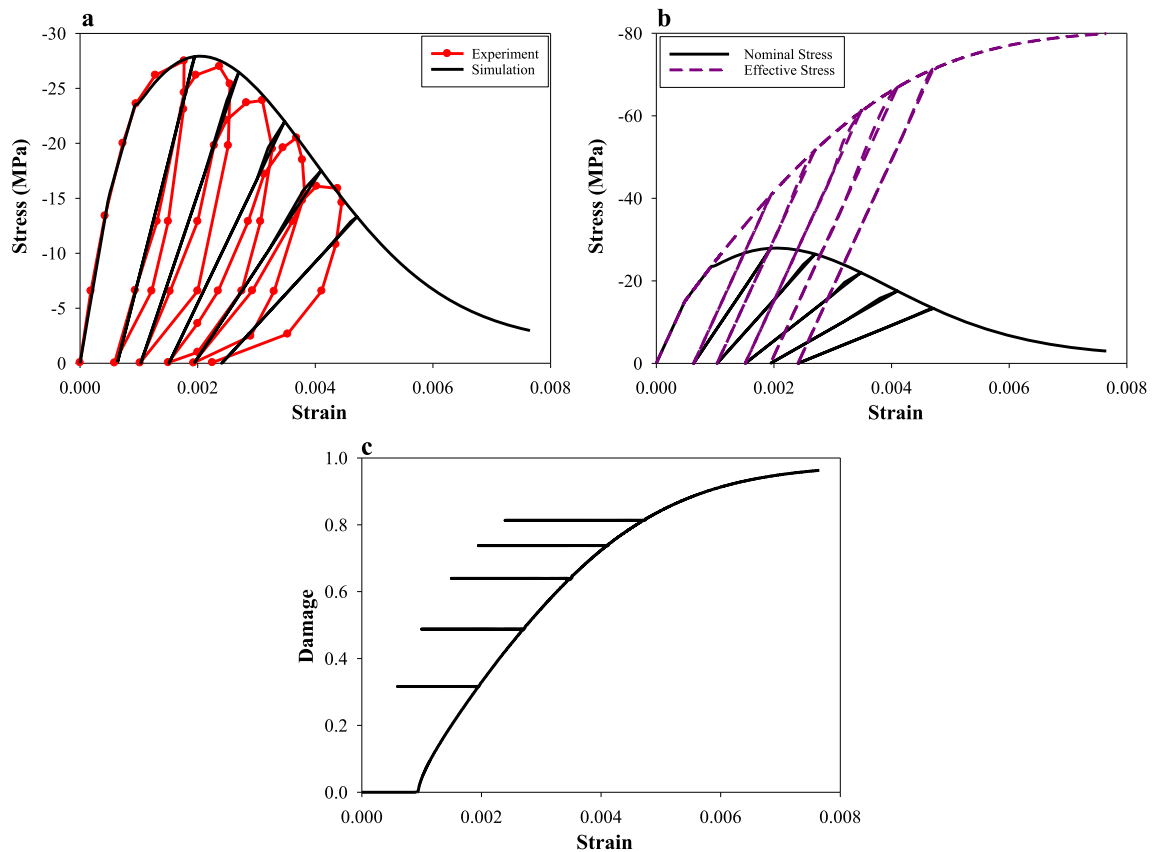


Fig. 10 Numerical results of cyclic uniaxial compressive test compared with Karsan and Jirsa [76]: **a** stress–strain curves, **b** comparison of nominal and effective stresses, **c** damage–strain curve

Table 11 Material properties

ν	\bar{E} (MPa)	f_0^+ (MPa)	h	K_0^+	B^+	q^+
0.2	38,000	2.9	600	0.0001	1.6	0.9

integration points. Due to the symmetric conditions, only half of the global structure is modeled. Figure 13 illustrates the beam’s geometry, boundary conditions, and loading arrangement. The material properties of concrete are also listed in Table 11. Figure 14 presents the load versus midspan deflection curves corresponding to the numerical and experimental tests. The exaggerated deformed shape of beam, including the employed mesh, is also illustrated in Fig. 15 in which the stretched elements show the crack pattern in the beam. The numerical results are compared with the experimental results of Hordijk [79]. The predicted load–deflection curve closely matches the curve obtained by experiment. The crack pattern is also in perfect agreement with the experimental result and shows the damage localization.

4.2.2 L-shaped concrete panel

The test performed by Winkler et al. [80] on an L-shaped concrete panel is adopted as the second structural test. The aim of this test is, first, to evaluate the accuracy and convergence of the solution and, second, to examine the model’s capabilities under dynamic loading conditions. Figure 16 illustrates the geometry and boundary condition of the model. The material parameters are also presented in Table 12. The simulated panel is analyzed with six different number of steps (62, 70, 86, 110, 120, and 125) to investigate the convergence of the algorithm. Figure 17 shows the force–displacement curves for the numerical and experimental solutions. Similar results are achieved from different analyses, which indicates robust convergence of the solution.

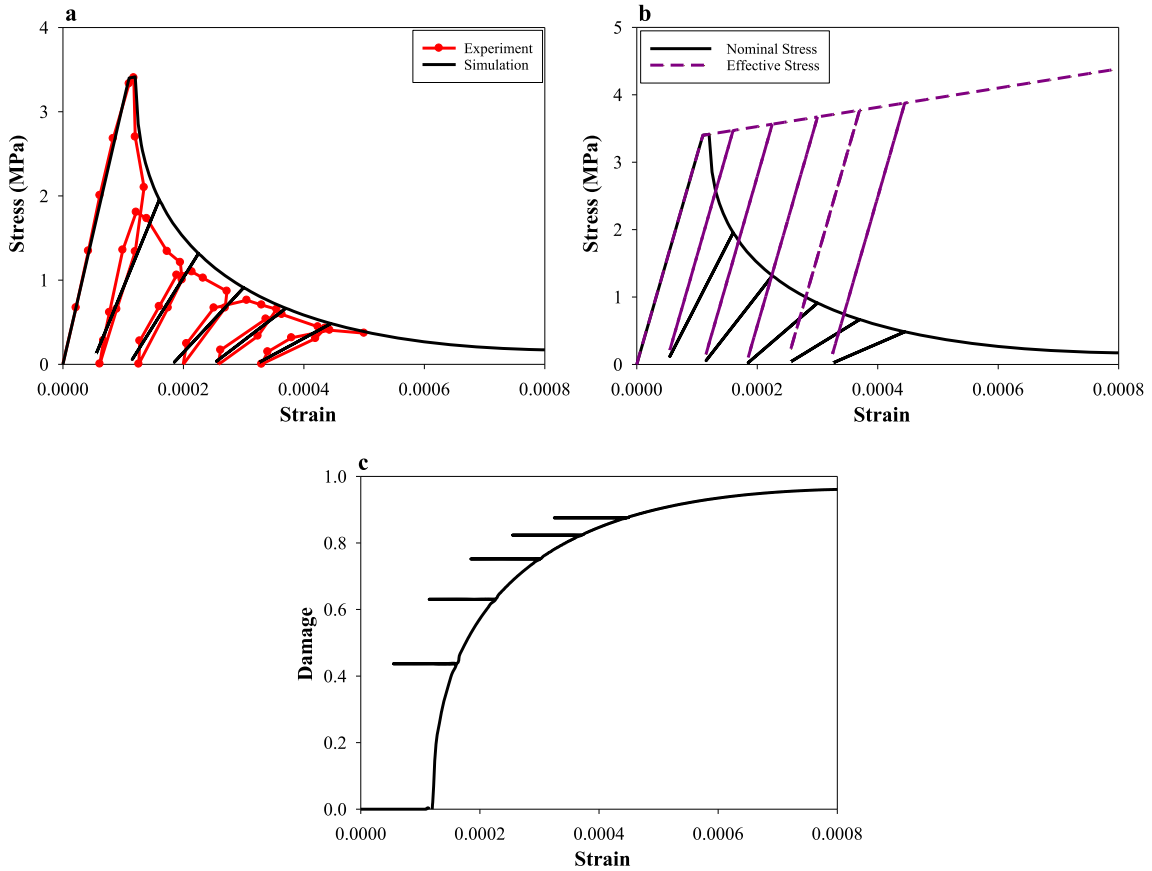


Fig. 11 Numerical results of cyclic uniaxial tensile test compared with Taylor [78]: **a** nominal stress–strain curves, **b** comparison of nominal and effective stresses, **c** damage–strain curve

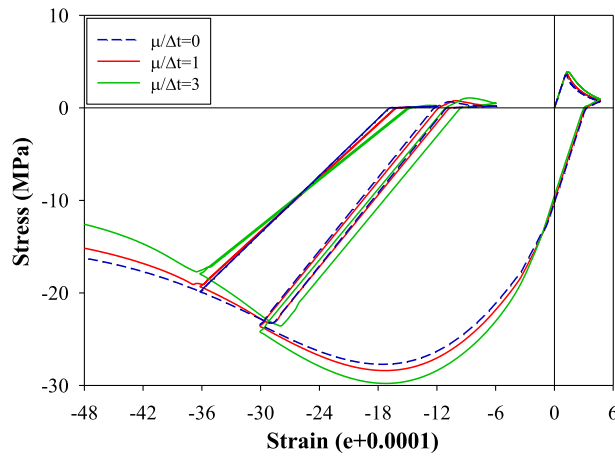


Fig. 12 Numerical stress–strain diagrams of full cyclic test in different viscosity ratios including large cracking possibility

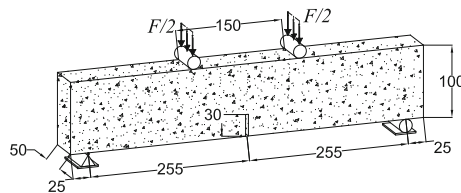


Fig. 13 Dimensions, boundary conditions, and loading arrangement of four-point bending test (unit: mm)

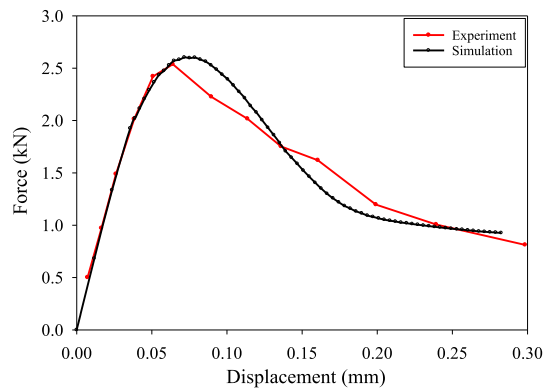


Fig. 14 Numerical solution of four-point bending test compared with experimental result of Hordijk [79]

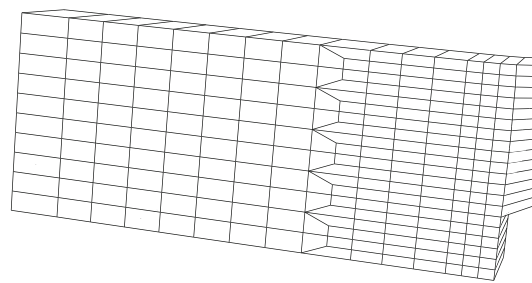


Fig. 15 Finite element mesh, deformed shape, and crack pattern of the simulated beam

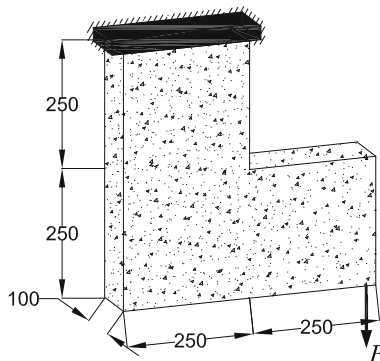


Fig. 16 The dimensions and boundary conditions of L-shaped concrete panel (unit: mm)

Table 12 Material properties

ν	\bar{E} (MPa)	f_0^+ (MPa)	h	K_0^+	B^+	q^+
0.2	23,000	2.7	600	0.000145	2.3	0.91

Finally, the panel is subjected to cyclic loading. The numerical and experimental force–displacement curves are plotted in Fig. 18, and the predicted crack trajectory and finite element mesh are illustrated in Fig. 19. Both the force–displacement curve and the crack pattern of the panel are in good agreement with the experimental data, which confirms the effectiveness of the model under cyclic loadings.

4.2.3 Four-point shear test

The four-point shear test of Arrea and Ingraffea [81] is adopted here to evaluate the abilities of the model under mixed-mode fracture. In this test, two point-loads (i.e., $P_1/P_2 = 0.13$) are applied to a notched beam

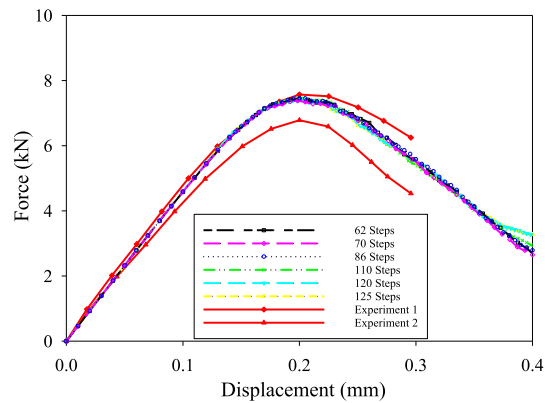


Fig. 17 Numerical solution of L-shaped concrete panel for five different number of steps

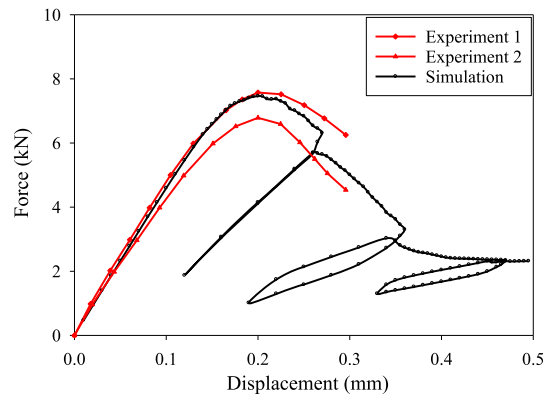


Fig. 18 Numerical solution of L-shaped concrete panel compared with experimental results of Winkler et al. [80]

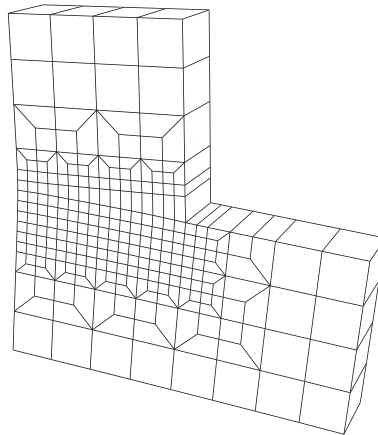


Fig. 19 Finite element mesh, deformed shape, and tensile crack pattern at the end of the analysis

through the indirect displacement control loading mode. The controlling parameter of loading is the relative vertical displacement of two notch sides, denoted as the “*crack mouth sliding displacement*” (CMSD), with an increment of 0.001 mm.

Figure 20 illustrates the beam’s dimensions, load conditions, and boundary conditions. Table 13 also presents the material parameters of the beam. The simulated beam includes 357 eight-node solid elements with eight integration points. The numerical and experimental force-CMSD curves are shown in Fig. 21. The predicted curve agrees well with the experimental results. In order to predict a more accurate crack trajectory, a second model with a finer mesh discretization is simulated and analyzed. The predicted deformed shapes

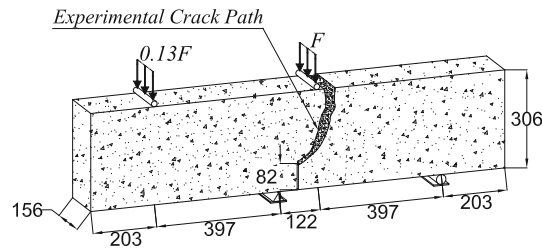


Fig. 20 Dimensions, boundary conditions, and experimental crack pattern of four-point shear test (unit: mm)

Table 13 Material properties

ν	\bar{E} (MPa)	f_0^+ (MPa)	h	K_0^+	B^+	q^+
0.18	29,000	2.8	2000	0.00016	1.8	0.85

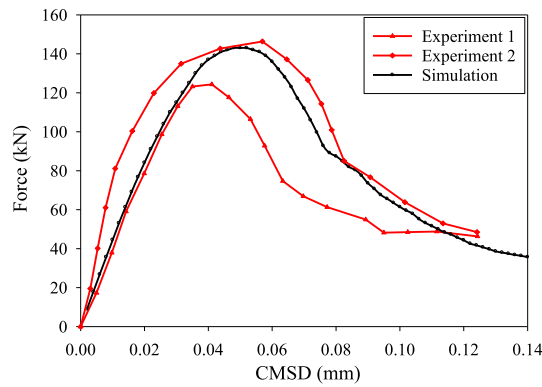


Fig. 21 Numerical solution of four-point shear test compared with experimental results of Arrea and Ingraffea [81]

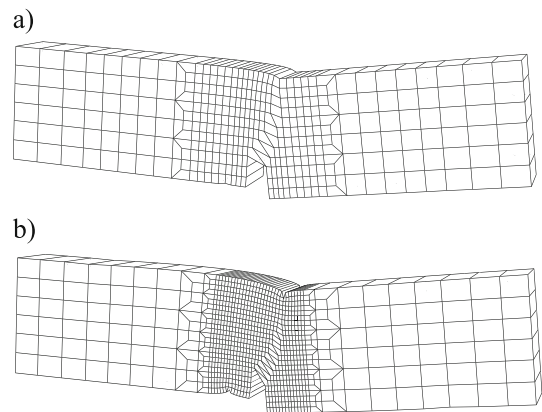


Fig. 22 Numerically predicted deformed shapes and crack trajectories for two finite element mesh types; **a** coarse mesh, **b** fine mesh

and crack trajectories are depicted in Fig. 22. In this test, a combination of fracture modes I and II with a curved crack path is anticipated. In both models, a curved crack starts from the tip of the notch and moves toward the nearest load application point. The crack trajectories of both models are in great agreement with experimental data, which confirms the abilities of the model to predict mixed-mode fracture with complicated crack patterns.

5 Summary and conclusions

In this paper, the formulation and finite element implementation techniques of a new ADPM model are presented for plain concrete, and the deficiencies of previous models are highlighted. A decoupled algorithm is used in the model to combine two powerful models of anisotropic damage and plasticity. The existing damage effect tensors in the literature are compared with respect to symmetry. The results reveal that some damage effect tensors unrealistically turn the uniaxial experiment to an equi-triaxial test in transition from effective to nominal configuration, and other examined tensors lead to unacceptable results or suffer from lack of minor symmetry. Hence, an improved relation that guarantees both the minor and major symmetry properties is used in the ADPM of this paper. In addition, two relations for damage hardening function (i.e., power and exponential relations) are presented and compared. Results of the model using the power relation closely match experimental data for both uniaxial and biaxial loadings, whereas the exponential relation, widely used in literature, fails to predict the experimental curve in the biaxial test, and its numerically obtained stress deviates from the experimental stress in the softening region.

Inspired by available models, three options are suggested and compared for the general formulation of the anisotropic damage model. Performance of the presented options is compared through uniaxial and biaxial experiments. The deficiencies of the first and second alternatives are demonstrated, and the third alternative is adopted for the damage formulation of the proposed ADPM model.

The formulation is extended to capture large crack opening and closing after the material point has experienced a threshold level of tensile damage. Moreover, the viscoplastic model of Duvaut–Lions is used to account for rate-dependent behavior of concrete. The numerical implementation of the model is also described in detail. In order to adopt a computationally efficient algorithm for calculation of damage hardening parameters, three computational methods are introduced and compared, including the methods used in literature and a new method proposed here. The methods are compared in terms of computational cost and experimental validation. The results clearly indicate that using the iterative algorithm for damage hardening parameters is unnecessary, and the proposed method is much more efficient than the iterative solutions presented in the literature.

The proposed ADPM model is implemented in an in-house finite element code. The numerical results obtained by the developed program are compared to those of experimental tests to investigate the efficiency of the model. Some benchmark problems, including single-element and structural tests in monotonic and cyclic loadings, are selected in this respect. The generated results perfectly agree with those obtained by experiments in all cases.

Funding No funding was received for conducting this study.

Declarations

Conflict of interest The authors have no relevant financial or non-financial interests to disclose.

Appendix A: The plastic multiplier

The plastic multiplier is determined using the plastic consistency condition:

$$\dot{f} = \frac{\partial f}{\partial \bar{\sigma}_{ij}} \dot{\bar{\sigma}}_{ij} + \frac{\partial f}{\partial \hat{\sigma}_{\max}} \dot{\hat{\sigma}}_{\max} + \frac{\partial f}{\partial \bar{\varepsilon}_{\text{eq}}^{-p}} \dot{\bar{\varepsilon}}_{\text{eq}}^{-p} + \frac{\partial f}{\partial \bar{\varepsilon}_{\text{eq}}^{+p}} \dot{\bar{\varepsilon}}_{\text{eq}}^{+p} = 0 \quad (\text{A1})$$

Using Eqs. (14), (18) and (A1), and after some manipulations, $\dot{\lambda}^P$ can be obtained as follows:

$$\Rightarrow \dot{\lambda}^P = \frac{\frac{\partial f}{\partial \bar{\sigma}_{ij}} \bar{E}_{ijkl} \dot{\varepsilon}_{kl} + \frac{\partial f}{\partial \hat{\sigma}_{\max}} \dot{\hat{\sigma}}_{\max} r}{\frac{\partial f}{\partial \bar{\sigma}_{ij}} \bar{E}_{ijkl} \frac{\partial F^P}{\partial \bar{\sigma}_{kl}} + \frac{\partial f}{\partial \hat{\sigma}_{\max}} \bar{E}_{11kl} \frac{\partial F^P}{\partial \hat{\sigma}_{kl}} + (1-r) \frac{\partial f}{\partial \bar{\varepsilon}_{\text{eq}}^{-p}} \frac{\partial F^P}{\partial \hat{\sigma}_{\min}} - r \frac{\partial f}{\partial \bar{\varepsilon}_{\text{eq}}^{+p}} \frac{\partial F^P}{\partial \hat{\sigma}_{\max}}} \quad (\text{A2})$$

In the above equation, the derivative of the plastic yield function with respect to effective stress $\frac{\partial f}{\partial \bar{\sigma}_{ij}}$ can be obtained as follows:

$$\frac{\partial f}{\partial \bar{\sigma}_{ij}} = \frac{\partial f}{\partial I_1} \frac{\partial I_1}{\partial \bar{\sigma}} + \frac{\partial f}{\partial \sqrt{J_2}} \frac{\partial \sqrt{J_2}}{\partial \bar{\sigma}} = \frac{3}{2} \frac{\bar{s}_{ij}}{\sqrt{3J_2}} + \alpha \delta_{ij} \quad (\text{A3})$$

Using Eqs. (14) and (15), the following relation can be obtained for the derivatives of yield criterion with respect to equivalent plastic strains:

$$\frac{\partial f}{\partial \bar{\varepsilon}_{\text{eq}}^{\pm p}} = \frac{\partial f}{\partial \bar{c}^{\pm}} \frac{\partial \bar{c}^{\pm}}{\partial \bar{\varepsilon}_{\text{eq}}^{\pm p}} \quad (\text{A4})$$

where $\partial f / \partial \bar{\varepsilon}_{\text{eq}}^{\pm p}$ can be determined from Eq. (14):

$$\begin{aligned} \frac{\partial f}{\partial \bar{\varepsilon}_{\text{eq}}^{-p}} &= (1 - \alpha) Q b \exp(-b \bar{\varepsilon}_{\text{eq}}^{-p}) \left[\frac{H(\hat{\sigma}_1) \hat{\sigma}_1}{\bar{c}^+} - 1 \right] \\ \frac{\partial f}{\partial \bar{\varepsilon}_{\text{eq}}^{+p}} &= -(1 - \alpha) H(\hat{\sigma}_1) \hat{\sigma}_1 \frac{\bar{c}^- h}{(\bar{c}^+)^2} \end{aligned} \quad (\text{A5})$$

The derivative of plastic potential function with respect to effective stress tensor is defined using Eq. (17):

$$\frac{\partial F^P}{\partial \bar{\sigma}_{ij}} = \frac{3}{2} \frac{\bar{s}_{ij}}{\sqrt{3J_2}} + \alpha^P \delta_{ij} \quad (\text{A6})$$

Appendix B: The damage multipliers

Similar to the plastic multiplier, the damage multipliers can be determined using the damage consistency condition:

$$\dot{g}^{\pm} = \frac{\partial g^{\pm}}{\partial Y_{mn}^{\pm}} \dot{Y}_{mn}^{\pm} + \frac{\partial g^{\pm}}{\partial K^{\pm}} \frac{\partial K^{\pm}}{\partial \varphi_{\text{eq}}^{\pm}} \dot{\varphi}_{\text{eq}}^{\pm} = 0 \quad (\text{B1})$$

Using Eqs. (B1) and (24), $\dot{\lambda}^{d\pm}$ can be obtained as follows:

$$\dot{\lambda}^{d\pm} = \frac{\frac{\partial g^{\pm}}{\partial Y_{mn}^{\pm}} \dot{Y}_{mn}^{\pm}}{-\beta \frac{\partial g^{\pm}}{\partial K^{\pm}} \frac{\partial K^{\pm}}{\partial \varphi_{\text{eq}}^{\pm}}} \quad (\text{B2})$$

where the increment of damage driving forces can be expressed as follows:

$$\dot{Y}_{mn}^{\pm} = \frac{\partial Y_{mn}^{\pm}}{\partial \sigma_{kl}^{\pm}} \dot{\sigma}_{kl}^{\pm} + \frac{\partial Y_{mn}^{\pm}}{\partial \varphi_{kl}^{\pm}} \dot{\varphi}_{kl}^{\pm}; \quad \dot{\varphi}_{kl}^{\pm} = \dot{\lambda}^{d\pm} \frac{\partial g^{\pm}}{\partial Y_{kl}^{\pm}} \quad (\text{B3})$$

Hence,

$$\dot{\lambda}^{d\pm} = \frac{\frac{\partial g^{\pm}}{\partial Y_{mn}^{\pm}} \frac{\partial Y_{mn}^{\pm}}{\partial \sigma_{kl}^{\pm}} M_{klrs}^{-1\pm} \dot{\sigma}_{rs}^{\pm}}{-\beta \frac{\partial g^{\pm}}{\partial K^{\pm}} \frac{\partial K^{\pm}}{\partial \varphi_{\text{eq}}^{\pm}} - \frac{\partial g^{\pm}}{\partial Y_{mn}^{\pm}} \frac{\partial Y_{mn}^{\pm}}{\partial \varphi_{kl}^{\pm}} \frac{\partial g^{\pm}}{\partial Y_{kl}^{\pm}} - \frac{\partial g^{\pm}}{\partial Y_{mn}^{\pm}} \frac{\partial Y_{mn}^{\pm}}{\partial \sigma_{kl}^{\pm}} \frac{\partial M_{klrs}^{-1\pm}}{\partial \varphi_{pq}^{\pm}} \frac{\partial g^{\pm}}{\partial Y_{pq}^{\pm}} \dot{\sigma}_{rs}^{\pm}} \quad (\text{B4})$$

where $\frac{\partial g^{\pm}}{\partial Y_{ij}^{\pm}}$ and $\frac{\partial g^{\pm}}{\partial K^{\pm}}$ can be obtained as follows:

$$\frac{\partial g^{\pm}}{\partial Y_{ij}^{\pm}} = \frac{L_{ijkl}^{\pm} Y_{kl}^{\pm}}{2\sqrt{\frac{1}{2} Y_{kl}^{\pm} L_{klmn}^{\pm} Y_{mn}^{\pm}}}; \quad \frac{\partial g^{\pm}}{\partial K^{\pm}} = -1 \quad (\text{B5})$$

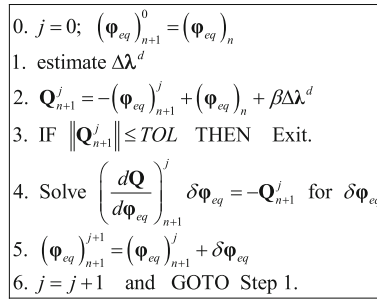


Fig. 23 The iterative algorithm for the calculation of $\Delta\lambda^{d\pm}$ and φ_{eq}^{\pm}

By taking the derivatives of Eq. (29) with respect to φ_{eq}^{\pm} the following relation can be obtained:

$$\frac{\partial K^{\pm}}{\partial \varphi_{eq}^{\pm}} = \frac{K_0^{\pm}}{B^{\pm} q^{\pm}} \left(\frac{\varphi_{eq}^{\pm}}{B^{\pm}} \right)^{\frac{1-q^{\pm}}{q^{\pm}}} \tag{B6}$$

According to Eq. (12), $\frac{\partial M_{ijkl}^{+-1}}{\partial \varphi_{mn}^{\pm}}$ is equal to:

$$\frac{\partial M_{ijkl}^{\pm-1}}{\partial \varphi_{mn}^{\pm}} = -\frac{1}{4} (\delta_{im}\delta_{kn}\delta_{jl} + \delta_{jm}\delta_{ik}\delta_{ln} + \delta_{jk}\delta_{im}\delta_{ln} + \delta_{il}\delta_{jm}\delta_{kn}) \tag{B7}$$

Since based on Eq. (12), $\partial^2 M_{ijpq}^{\pm-1} / \partial \varphi_{rs}^{\pm 2} = 0$, hence, $\partial Y_{ij}^{\pm} / \partial \varphi_{kl}^{\pm}$ can be calculated using Eq. (20) and strain equivalence hypothesis:

$$\frac{\partial Y_{rs}^{\pm}}{\partial \varphi_{kl}^{\pm}} = -\frac{1}{2} E_{ijab}^{-1} \bar{\sigma}_{ab} \frac{\partial^2 M_{ijpq}^{\pm-1}}{\partial \varphi_{rs}^{\pm} \partial \varphi_{kl}^{\pm}} \bar{\sigma}_{pq}^{\pm} = 0 \tag{B8}$$

Additionally, $\frac{\partial Y_{ij}^{\pm}}{\partial \sigma_{kl}^{\pm}}$ can be obtained as follows:

$$\frac{\partial Y_{ij}^{\pm}}{\partial \sigma_{kl}^{\pm}} = \frac{\partial Y_{ij}^{\pm}}{\partial \sigma_{mn}^{\pm}} \frac{\partial \bar{\sigma}_{mn}^{\pm}}{\partial \sigma_{kl}^{\pm}} = \left(-\frac{1}{2} E_{urmn}^{-1} \frac{\partial M_{urpq}^{+-1}}{\partial \varphi_{ij}^{\pm}} \bar{\sigma}_{pq}^{\pm} + -\frac{1}{2} E_{urab}^{-1} \bar{\sigma}_{ab}^{\pm} \frac{\partial M_{urmn}^{+-1}}{\partial \varphi_{ij}^{\pm}} \right) M_{mnkl}^{\pm} \tag{B9}$$

Since $\frac{\partial K^{\pm}}{\partial \varphi_{eq}^{\pm}}$ in Eq. (B4) is a function of φ_{eq}^{\pm} and subsequently $\Delta\lambda^{d\pm}$ is a function of φ_{eq}^{\pm} and φ_{ij}^{\pm} , an iterative solution scheme is needed to calculate $\Delta\lambda^{d\pm}$. This iterative algorithm is described in Fig. 23.

References

1. Menetrey, P., Willam, K.J.: Triaxial failure criterion for concrete and its generalization. ACI Struct. J. (1995). <https://doi.org/10.14359/1132>
2. Oñate, E., Oller, S., Oliver, J., Lubliner, J.: A constitutive model for cracking of concrete based on the incremental theory of plasticity. Eng. Comput. **5**, 309–319 (1988). <https://doi.org/10.1108/eb023750>
3. Pramono, E., Willam, K.: Fracture energy-based plasticity formulation of plain concrete. J. Eng. Mech. (ASCE) **115**(6), 1183–1204 (1989)
4. Farahat, A.M., Kawakami, M., Ohtsu, M.: Strain-space plasticity model for the compressive hardening-softening behaviour of concrete. Constr. Build. Mater. **9**, 45–59 (1995). [https://doi.org/10.1016/0950-0618\(95\)92860-J](https://doi.org/10.1016/0950-0618(95)92860-J)
5. Karavelić, E., Ibrahimbegovic, A., Dolarević, S.: Multi-surface plasticity model for concrete with 3D hardening/softening failure modes for tension, compression and shear. Comput. Struct. **221**, 74–90 (2019). <https://doi.org/10.1016/J.COMPSTRUC.2019.05.009>
6. Mazars, J., Hamon, F., Grange, S.: A new 3D damage model for concrete under monotonic, cyclic and dynamic loadings. Mater. Struct. **48**, 3779–3793 (2014). <https://doi.org/10.1617/s11527-014-0439-8>
7. Tao, X., Phillips, D.V.: A simplified isotropic damage model for concrete under bi-axial stress states. Cem. Concr. Compos. **27**, 716–726 (2005). <https://doi.org/10.1016/j.cemconcomp.2004.09.017>

8. He, W., Wu, Y.-F., Xu, Y., Fu, T.-T.: A thermodynamically consistent nonlocal damage model for concrete materials with unilateral effects. *Comput. Methods Appl. Mech. Eng.* **297**, 371–391 (2015). <https://doi.org/10.1016/j.cma.2015.09.010>
9. Ren, Y., Chen, J., Lu, G.: A structured deformation driven nonlocal macro-meso-scale consistent damage model for the compression/shear dominate failure simulation of quasi-brittle materials. *Comput. Methods Appl. Mech. Eng.* **410**, 115945 (2023). <https://doi.org/10.1016/J.CMA.2023.115945>
10. Evangelista, F., Alves, G.S., Moreira, J.F.A., Paiva, G.O.F.: A global–local strategy with the generalized finite element framework for continuum damage models. *Comput. Methods Appl. Mech. Eng.* **363**, 112888 (2020). <https://doi.org/10.1016/J.CMA.2020.112888>
11. Brekelmans, W.A.M., de Vree, J.H.P.: Reduction of mesh sensitivity in continuum damage mechanics. *Acta Mech.* **110**, 49–56 (1995). <https://doi.org/10.1007/BF01215415/METRICS>
12. Solanki, K.N., Bammann, D.J.: A thermodynamic framework for a gradient theory of continuum damage. *Acta Mech.* **213**, 27–38 (2010). <https://doi.org/10.1007/S00707-009-0200-5/METRICS>
13. Clayton, J.D., Freed, A.D.: A constitutive framework for finite viscoelasticity and damage based on the Gram-Schmidt decomposition. *Acta Mech.* **231**, 3319–3362 (2020). <https://doi.org/10.1007/S00707-020-02689-5/METRICS>
14. Brüning, M., Michalski, A.: A stress-state-dependent continuum damage model for concrete based on irreversible thermodynamics. *Int. J. Plast.* **90**, 31–43 (2017). <https://doi.org/10.1016/j.ijplas.2016.12.002>
15. de Borst, R.: Fracture and damage in quasi-brittle materials: A comparison of approaches. *Theoret. Appl. Fract. Mech.* **122**, 103652 (2022). <https://doi.org/10.1016/J.TAFMEC.2022.103652>
16. Farahani, B.V., Belinha, J., Pires, F.M.A., Ferreira, A.J.M., Moreira, P.M.G.P.: A meshless approach to non-local damage modelling of concrete. *Eng. Anal. Bound. Elem.* **79**, 62–74 (2017). <https://doi.org/10.1016/J.ENGANABOUND.2017.04.002>
17. De-Pouplana, I., Oñate, E.: Combination of a non-local damage model for quasi-brittle materials with a mesh-adaptive finite element technique. *Finite Elem. Anal. Des.* **112**, 26–39 (2016). <https://doi.org/10.1016/J.FINEL.2015.12.011>
18. Resende, L.: A Damage mechanics constitutive theory for the inelastic behaviour of concrete. *Comput. Methods Appl. Mech. Eng.* **60**, 57–93 (1987). [https://doi.org/10.1016/0045-7825\(87\)90130-7](https://doi.org/10.1016/0045-7825(87)90130-7)
19. Challamel, N., Lanos, C., Casandjian, C.: Creep failure of a simply supported beam through a uniaxial Continuum Damage Mechanics model. *Acta Mech.* **192**, 213–234 (2007). <https://doi.org/10.1007/S00707-007-0453-9/METRICS>
20. Hütter, M., Tervoort, T.A.: Continuum damage mechanics: Combining thermodynamics with a thoughtful characterization of the microstructure. *Acta Mech.* **201**, 297–312 (2008). <https://doi.org/10.1007/S00707-008-0064-0/METRICS>
21. Zafati, E., Richard, B.: Anisotropic continuum damage constitutive model to describe the cyclic response of quasi-brittle materials: The regularized unilateral effect. *Int. J. Solids Struct.* **162**, 164–180 (2019). <https://doi.org/10.1016/J.IJSOLSTR.2018.12.009>
22. Wang, G., Lu, D., Zhou, X., Wu, Y., Du, X., Xiao, Y.: A stress-path-independent damage variable for concrete under multiaxial stress conditions. *Int. J. Solids Struct.* **206**, 59–74 (2020). <https://doi.org/10.1016/J.IJSOLSTR.2020.09.012>
23. Rodríguez-Ferran, A., Morata, I., Huerta, A.: Efficient and reliable nonlocal damage models. *Comput. Methods Appl. Mech. Eng.* **193**, 3431–3455 (2004). <https://doi.org/10.1016/J.CMA.2003.11.015>
24. Stanić, A., Brank, B., Brancherie, D.: Fracture of quasi-brittle solids by continuum and discrete-crack damage models and embedded discontinuity formulation. *Eng. Fract. Mech.* **227**, 106924 (2020). <https://doi.org/10.1016/J.ENGFRACMECH.2020.106924>
25. Wu, J.-Y., Cervera, M.: A novel positive/negative projection in energy norm for the damage modeling of quasi-brittle solids. *Int. J. Solids Struct.* **139–140**, 250–269 (2018). <https://doi.org/10.1016/j.ijsolstr.2018.02.004>
26. Brüning, M., Gerke, S., Schmidt, M.: Damage and failure at negative stress triaxialities: Experiments, modeling and numerical simulations. *Int. J. Plast.* **102**, 70–82 (2018). <https://doi.org/10.1016/J.IJPLAS.2017.12.003>
27. Zhu, Q.Z., Shao, J.F., Kondo, D.: A micromechanics-based thermodynamic formulation of isotropic damage with unilateral and friction effects. *Eur. J. Mech. A. Solids* **30**, 316–325 (2011). <https://doi.org/10.1016/J.EUROMECHSOL.2010.12.005>
28. Narayan, S., Anand, L.: A gradient-damage theory for fracture of quasi-brittle materials. *J. Mech. Phys. Solids* **129**, 119–146 (2019). <https://doi.org/10.1016/J.JMPS.2019.05.001>
29. Lubliner, J., Oliver, J., Oller, S., Oñate, E.: A plastic-damage model for concrete. *Int. J. Solids Struct.* **25**, 299–326 (1989). [https://doi.org/10.1016/0020-7683\(89\)90050-4](https://doi.org/10.1016/0020-7683(89)90050-4)
30. Lee, J., Fenves, G.L.: Plastic-damage model for cyclic loading of concrete structures. *J. Eng. Mech.* **124**, 892–900 (1998). [https://doi.org/10.1061/\(ASCE\)0733-9399\(1998\)124:8\(892\)](https://doi.org/10.1061/(ASCE)0733-9399(1998)124:8(892))
31. Voyiadjis, G.Z., Taqieddin, Z.N.: Elastic plastic and damage model for concrete materials: part I-theoretical formulation. *Int. J. Struct. Changes Solids*. **1**(1), 31–59 (2009)
32. Lotfí, V., Omidí, O.: Dynamic analysis of the Koyna dam using three-dimensional plastic-damage modelling. *J. Dam Eng.* **22**(3), 197 (2012)
33. Zhou, X., Lu, D., Du, X., Wang, G., Meng, F.: A 3D non-orthogonal plastic damage model for concrete. *Comput. Methods Appl. Mech. Eng.* **360**, 112716 (2020). <https://doi.org/10.1016/J.CMA.2019.112716>
34. Wu, J.Y., Li, J., Faria, R.: An energy release rate-based plastic-damage model for concrete. *Int. J. Solids Struct.* **43**, 583–612 (2006). <https://doi.org/10.1016/j.ijsolstr.2005.05.038>
35. Nguyen, G.D., Korsunsky, A.M.: Development of an approach to constitutive modelling of concrete: Isotropic damage coupled with plasticity. *Int. J. Solids Struct.* **45**, 5483–5501 (2008). <https://doi.org/10.1016/j.ijsolstr.2008.05.029>
36. Niu, Y., Wang, W., Su, Y., Jia, F., Long, X.: Plastic damage prediction of concrete under compression based on deep learning. *Acta Mech.* (2023). <https://doi.org/10.1007/S00707-023-03743-8/METRICS>
37. Li, Y., He, X., Sun, H., Tan, Y.: Research on viscoelastic-plastic damage characteristics of cement asphalt composite binder. *Constr. Build. Mater.* **274**, 122064 (2021). <https://doi.org/10.1016/J.CONBUILDMAT.2020.122064>
38. Frantziskonis, G., Desai, C.S.: Elastoplastic model with damage for strain softening geomaterials. *Acta Mech.* **68**, 151–170 (1987). <https://doi.org/10.1007/BF01190880/METRICS>
39. Grassl, P., Xenos, D., Nyström, U., Rempling, R., Gylltoft, K.: CDPM2: a damage-plasticity approach to modelling the failure of concrete. *Int. J. Solids Struct.* **50**, 3805–3816 (2013). <https://doi.org/10.1016/j.ijsolstr.2013.07.008>

40. Omidi, O., Lotfi, V.: Finite element analysis of concrete structures using plastic-damage model in 3-d implementation. *Int. J. Civ. Eng.* **8**, 187–203 (2010)
41. Dimitrov, N., Liu, Y., Horstemeyer, M.F.: On the thermo-mechanical coupling of the Bammann plasticity-damage internal state variable model. *Acta Mech.* **230**, 1855–1868 (2019). <https://doi.org/10.1007/S00707-019-2365-X/METRICS>
42. Mohammadi, M., Wu, Y.F.: Modified plastic-damage model for passively confined concrete based on triaxial tests. *Compos. B Eng.* **159**, 211–223 (2019). <https://doi.org/10.1016/J.COMPOSITESB.2018.09.074>
43. Wang, M., Cormery, F., Shen, W., Shao, J.: A novel phase-field model for mixed cracks in elastic–plastic materials incorporating unilateral effect and friction sliding. *Comput. Methods Appl. Mech. Eng.* **405**, 115869 (2023). <https://doi.org/10.1016/J.CMA.2022.115869>
44. Zhao, L., Zhang, L., Mao, J., Liu, Z.: An elastoplastic damage model of concrete under cyclic loading and its numerical implementation. *Eng. Fract. Mech.* **273**, 108714 (2022). <https://doi.org/10.1016/J.ENGFRACTMECH.2022.108714>
45. Wosatko, A., Genikomsou, A., Pamin, J., Polak, M.A., Winnicki, A.: Examination of two regularized damage-plasticity models for concrete with regard to crack closing. *Eng. Fract. Mech.* **194**, 190–211 (2018). <https://doi.org/10.1016/J.ENGFRACTMECH.2018.03.002>
46. Salsavilca, J., Tarque, N., Yacila, J., Camata, G.: Numerical analysis of bonding between masonry and steel reinforced grout using a plastic–damage model for lime–based mortar. *Constr. Build. Mater.* **262**, 120373 (2020). <https://doi.org/10.1016/J.CONBUILDMAT.2020.120373>
47. Xotta, G., Beizae, S., Willam, K.J.: Bifurcation investigations of coupled damage-plasticity models for concrete materials. *Comput. Methods Appl. Mech. Eng.* **298**, 428–452 (2016). <https://doi.org/10.1016/J.CMA.2015.10.010>
48. Jason, L., Huerta, A., Pijaudier-Cabot, G., Ghavami, S.: An elastic plastic damage formulation for concrete: Application to elementary tests and comparison with an isotropic damage model. *Comput. Methods Appl. Mech. Eng.* **195**, 7077–7092 (2006). <https://doi.org/10.1016/j.cma.2005.04.017>
49. Grassl, P., Jirásek, M.: Damage-plastic model for concrete failure. *Int. J. Solids Struct.* **43**, 7166–7196 (2006). <https://doi.org/10.1016/j.ijsolstr.2006.06.032>
50. Zhao, L.Y., Zhu, Q.Z., Shao, J.F.: A micro-mechanics based plastic damage model for quasi-brittle materials under a large range of compressive stress. *Int. J. Plast.* **100**, 156–176 (2018). <https://doi.org/10.1016/J.IJPLAS.2017.10.004>
51. Park, T., Ahmed, B., Voyiadjis, G.Z.: A review of continuum damage and plasticity in concrete: part I—theoretical framework. *Int. J. Damage Mech* **31**, 901–954 (2022). <https://doi.org/10.1177/10567895211068174>
52. Voyiadjis, G.Z., Ahmed, B., Park, T.: A review of continuum damage and plasticity in concrete: part II—numerical framework. *Int. J. Damage Mech* **31**, 762–794 (2022). <https://doi.org/10.1177/10567895211063227>
53. Unger, J.F., Eckardt, S.: Multiscale modeling of concrete. *Arch. Comput. Methods Eng.* **18**(3), 341–393 (2011). <https://doi.org/10.1007/S11831-011-9063-8>
54. Cicekli, U., Voyiadjis, G.Z., Abu Al-Rub, R.K.: A plasticity and anisotropic damage model for plain concrete. *Int. J. Plast.* **23**, 1874–1900 (2007). <https://doi.org/10.1016/j.ijplas.2007.03.006>
55. Voyiadjis, G.Z., Taqieddin, Z.N., Kattan, P.I.: Anisotropic damage–plasticity model for concrete. *Int. J. Plast.* **24**, 1946–1965 (2008). <https://doi.org/10.1016/j.ijplas.2008.04.002>
56. Voyiadjis, G.Z., Taqieddin, Z.N., Kattan, P.I.: Theoretical formulation of a coupled elastic—plastic anisotropic damage model for concrete using the strain energy equivalence concept. *Int. J. Damage Mech* **18**, 603–638 (2009). <https://doi.org/10.1177/1056789508092399>
57. Abu Al-Rub, R.K., Voyiadjis, G.Z.: Gradient-enhanced coupled plasticity-anisotropic damage model for concrete fracture: computational aspects and applications. *Int. J. Damage Mech* **18**, 115–154 (2009). <https://doi.org/10.1177/1056789508097541>
58. Voyiadjis, G.Z., Zhou, Y., Kattan, P.I.: A new anisotropic elasto-plastic-damage model for quasi-brittle materials using strain energy equivalence. *Mech. Mater.* **165**, 104163 (2022). <https://doi.org/10.1016/J.MECHMAT.2021.104163>
59. Daneshyar, A., Ghaemian, M.: Coupling microplane-based damage and continuum plasticity models for analysis of damage-induced anisotropy in plain concrete. *Int. J. Plast.* **95**, 216–250 (2017). <https://doi.org/10.1016/j.ijplas.2017.04.011>
60. Zhang, J., Li, J., Ju, J.W.: 3D elastoplastic damage model for concrete based on novel decomposition of stress. *Int. J. Solids Struct.* **94–95**, 125–137 (2016). <https://doi.org/10.1016/j.ijsolstr.2016.04.038>
61. Lee, J., Fenves, G.L.: A plastic-damage concrete model for earthquake analysis of dams. *Earthq. Eng. Struct. Dyn.* **27**, 937–956 (1998). [https://doi.org/10.1002/\(SICI\)1096-9845\(199809\)27:9%3c937::AID-EQE764%3e3.0.CO;2-5](https://doi.org/10.1002/(SICI)1096-9845(199809)27:9%3c937::AID-EQE764%3e3.0.CO;2-5)
62. Voyiadjis, G.Z., Kattan, P.I.: *Advances in Damage Mechanics: Metals and Metal Matrix Composites with an Introduction to Fabric Tensors*. Elsevier, Amsterdam (2006)
63. Voyiadjis, G.Z., Kattan, P.I.: A plasticity-damage theory for large deformation of solids—I. Theoretical formulation. *Int. J. Eng. Sci.* **30**, 1089–1108 (1992). [https://doi.org/10.1016/0020-7225\(92\)90059-P](https://doi.org/10.1016/0020-7225(92)90059-P)
64. Voyiadjis, G.Z., Park, T.: Anisotropic damage effect tensors for the symmetrization of the effective stress tensor. *J. Appl. Mech.* **64**, 106–110 (1997). <https://doi.org/10.1115/1.2787259>
65. Cordebois, J.P., Sidoroff, F.: Damage induced elastic anisotropy. In *Mechanical Behavior of Anisotropic Solids/Comportment Mécanique des Solides Anisotropes*. pp. 761–774. Springer Netherlands, Dordrecht (1982)
66. Abu Al-Rub, R.K., Kim, S.-M.: Computational applications of a coupled plasticity-damage constitutive model for simulating plain concrete fracture. *Eng. Fract. Mech.* **77**, 1577–1603 (2010). <https://doi.org/10.1016/j.engfracmech.2010.04.007>
67. Taqieddin, Z.N.: *Elasto-Plastic and Damage Modeling of Reinforced Concrete*, (2008)
68. Abu Al-Rub, R.K., Voyiadjis, G.Z.: On the coupling of anisotropic damage and plasticity models for ductile materials. *Int. J. Solids Struct.* **40**, 2611–2643 (2003). [https://doi.org/10.1016/S0020-7683\(03\)00109-4](https://doi.org/10.1016/S0020-7683(03)00109-4)
69. Cicekli, U.: *A Plasticity-Damage Model for Plain Concrete*, (2006)
70. Abu Al-Rub, R.K.: *Material Length Scales in Gradient-Dependent Plasticity/Damage and Size Effects: Theory and Computation* (2004)
71. Chow, C.L., Wang, J.: An anisotropic theory of elasticity for continuum damage mechanics. *Int. J. Fract.* **33**, 3–16 (1987). <https://doi.org/10.1007/BF00034895>
72. Kupfer, H., Hilsdorf, H.K., Rusch, H.: Behavior of concrete under biaxial stresses. *Am. Concr. Inst. J.* **66**(8), 656–666 (1969)

73. Zhu, Q.Z., Zhao, L.Y., Shao, J.F.: Analytical and numerical analysis of frictional damage in quasi brittle materials. *J. Mech. Phys. Solids* **92**, 137–163 (2016). <https://doi.org/10.1016/j.jmps.2016.04.002>
74. Omidi, O., Lotfi, V.: Continuum large cracking in a rate-dependent plastic-damage model for cyclic-loaded concrete structures. *Int. J. Numer. Anal. Methods Geomech.* **37**, 1363–1390 (2013). <https://doi.org/10.1002/nag.2093>
75. Lee, J., Fenves, G.L.: A return-mapping algorithm for plastic-damage models: 3-D and plane stress formulation. *Int. J. Numer. Methods Eng.* **50**, 487–506 (2001). [https://doi.org/10.1002/1097-0207\(20010120\)50:2%3c487::AID-NME44%3e3.0.CO;2-N](https://doi.org/10.1002/1097-0207(20010120)50:2%3c487::AID-NME44%3e3.0.CO;2-N)
76. Karsan, I.D., Jirsa, J.O.: Behavior of concrete under compressive loadings. *J. Struct. Div.* **95**, 2543–2564 (1969). <https://doi.org/10.1061/JSDEAG.0002424>
77. Zhang, Q.Y.: Research on the stochastic damage constitutive of concrete material, (2001)
78. Taylor, R.L.: FEAP: A finite element analysis program for engineering workstation. Rep. No. UCB/SEMM-92 (Draft version). (1992)
79. Hordijk, D.A.: Local approach to fatigue of concrete, (1991)
80. Winkler, B., Hofstetter, G., Niederwanger, G.: Experimental verification of a constitutive model for concrete cracking. *Proc. Inst. Mech. Eng. Part L J. Mater. Des. Appl.* **215**, 75–86 (2001). <https://doi.org/10.1177/146442070121500202>
81. Arrea, M., Ingraffea, A.: Mixed mode crack propagation in mortar and concrete, New York (1982)

Publisher's Note Springer Nature remains neutral with regard to jurisdictional claims in published maps and institutional affiliations.

Springer Nature or its licensor (e.g. a society or other partner) holds exclusive rights to this article under a publishing agreement with the author(s) or other rightsholder(s); author self-archiving of the accepted manuscript version of this article is solely governed by the terms of such publishing agreement and applicable law.